KINEMATICS OF AND EMISSION FROM HELICALLY ORBITING BLOBS
IN A RELATIVISTIC MAGNETIZED JET

P. MOHAN[1,2] AND A. MANGALAM[1]
[1] Indian Institute of Astrophysics, Sarjapur Road, Koramangala, Bangalore, 560034, India; prashanth@iiap.res.in
[2] Aryabhatta Research Institute of Observational Sciences, Manora Peak, Nainital, 263002, India; mangalam@iiap.res.in

ABSTRACT

We present a general relativistic (GR) model of jet variability in active galactic nuclei due to orbiting blobs in helical motion along a funnel or cone-shaped magnetic surface anchored to the accretion disk near the black hole. Considering a radiation pressure driven flow in the inner region, we find that it stabilizes the flow, yielding Lorentz factors ranging between 1.1 and 7 at small radii for reasonable initial conditions. Assuming these as inputs, simulated light curves (LCs) for the funnel model include Doppler and gravitational shifts, aberration, light bending, and time delay. These LCs are studied for quasi-periodic oscillations (QPOs) and the power spectral density (PSD) shape, and yield an increased amplitude ($\sim$12%), a beamed portion and a systematic phase shift with respect to that from a previous special relativistic model. The results strongly justify implementing a realistic magnetic surface geometry in Schwarzschild geometry to describe effects on emission from orbital features in the jet close to the horizon radius. A power-law-shaped PSD with a typical slope of −2 and QPOs with timescales in the range of (1.37–130.7) days consistent with optical variability in blazars, emerges from the simulations for black hole masses $M_\bullet = (0.5-5) \times 10^8 \, M_\odot$ and initial Lorentz factors $\gamma_{\rm jet,i} = 2-10$. The models presented here can be applied to explain radio, optical, and X-ray variability from a range of jetted sources including active galactic nuclei, X-ray binaries, and neutron stars.

Key words: accretion, accretion disks – black hole physics – BL Lacertae objects: general – galaxies: active – galaxies: jets – pulsars: general

1. INTRODUCTION

A bulk flowing plasma close to the innermost stable circular orbit (ISCO) of a black hole, consisting of the accretion disk and developing jet, is strongly influenced by magnetic field structures, differential rotation of the disk, and radiative structuring. The flow velocity field and magnetic fields are dominated by the azimuthal and possibly the radial components. The poloidal components are non-zero owing to vertical structuring, random motions, radiation pressure, and dynamo action in the disk. The magnetic field strength generated by dynamo action in the inner disk is expected to be in equipartition with the gas pressure (e.g., Brandenburg et al. 1995), allowing for a reasonably well-developed vertical structuring in the field (Spruit 1996).

Variability is often observed in emission from active galactic nuclei (AGNs) with strong jet components such as blazars, inferred from the domination of synchrotron processes in radio to optical light curves (LCs) and spectra from regions at parsec scales as well as close to the base of the jet (e.g., Wagner et al. 1996; Gupta et al. 2012). Theoretical models are often applicable to emission from regions that are some distance away from the central region where structures are resolvable. Some of these include Doppler beaming of a stream or blobs of plasma accelerated to relativistic velocities along helical paths (Camenzind & Krockenberger 1992; Steffen et al. 1995; Rieger 2004), as was recently observed in the blazar BL Lacertae (Marscher et al. 2008), and shocks propagating along the relativistic jet (Marscher & Gear 1985), which explains the variability in some blazars (e.g., Qian et al. 1991; Hagen-Thorn et al. 2008). Quasi-periodic variability can be caused due to the orbital motion of the flow along helical trajectories which get beamed when their local angle is close to the angle to the observer's line of sight in the inner region where the jet is just developing. This effect is expected to last for a few cycles.

In a study of X-ray binaries, the inner jet appears to be intrinsically linked to the corona because spectral characteristics of its emissions are the same as those from a Comptonized corona (Markoff et al. 2005). In another study, VLBI observations at 1.3 mm resolve structures and study the emission from the inner jet of M87 (Doeleman et al. 2012). In this study, a direct scaling relation between the angular size and the distance to the object indicates that the region of emission is very compact, even inside of the ISCO ($5.5 \pm 0.4 \, R_s$, where R_s is the Schwarzschild radius), implying that the emitting source is on a prograde orbit. These and similar studies indicate that there is a strong disk–jet connection, which is also likely because perturbations produced in the disk can be advected into the jet and amplified there via Doppler boosting (e.g., Wiita 2006).

Emission in AGNs such as blazars is observed in a wide variety of wavelengths ranging from radio to optical to Gamma-rays (e.g., Abdo et al. 2011) and can be inferred in many cases to arise from the jet. Intra-day variability in the optical bands is frequently observed in strongly jetted radio-loud AGNs. The measured magnitude often changes by an order or more in less than a day (e.g., Gupta et al. 2008). Jet variability in the X-rays is observed on timescales of a few hours. A possible 4.6 hr QPO in an X-ray LC of the blazar PKS 2155-304 and the interpretation is discussed in terms of instabilities in the disk being advected into the jet and intrinsic jet-based processes including shocks in jets (Lachowicz et al. 2009). IDV timescales ranging between 15.7 and 46.8 ks have been detected in eight LCs from 1ES 1426+428 and

PKS 2155-304 (Gaur et al. 2010). Intra-night variability in the optical B and R bands have detected timescales ranging from several hours to a week in the radio loud narrow line Seyfert 1 galaxy SDSS J094857.3+002225, interpreted in terms of physical processes in a relativistic jet (Liu et al. 2010). These and other studies indicate that short-term (a few hours) to long-term (a few days to weeks) variability is commonly observed in radio, optical, and X-ray wavelengths. A helical kinematical jet model was applied to explain the trajectories of blobs in the inner jet (Steffen et al. 1995). In the study, the model is applied to quasar 3C 345 to infer an inclination angle of 6°.8 and typical Lorentz factors of 5.8 and 4.6 for two radio components.

In our paper, we define "blobs" to be density inhomogeneities that are acted upon by the centrifugal force, radiation pressure and drag, and the gravitational force of the black hole. We, however, do not include any thermodynamic evolution of the blob. The blob flows along with the bulk plasma in the region with a dominant magnetic field, where the plasma is constrained by flux freezing to flow along the magnetic surface encompassing the jet. The variability could be attributed to orbital blobs propagating along the jet, the emission from which is beamed along the observer's line of sight causing rapid changes in the received flux. Our model assumes a flow that has transited from the accretion disk onto the jet through the magnetic field surface anchored onto the disk at foot points close to the black hole. Thus, blobs such as orbiting spots could be present in the jet at various scales in the mass-loaded jet. This is expected to occur regardless of the jet models such as the purely electro-magnetic jets or the magnetohydrodynamic jets. The developed model is used to study the quasi-periodic oscillations (QPOs) phenomenon in addition to the timing study of simulated LCs using the Fourier periodogram and wavelet analysis. Our model can be used to study both the timing properties and the variable emission from orbiting blobs as well as model the jet structure and place constraints on the trajectories of these orbiting blobs, which can be compared with observations.

Earlier works in this direction have mainly addressed only accretion disk based variability and its timing properties. Models include the variability due to orbiting blobs and are applicable to optical/UV and X-ray wavelengths (e.g., Zhang & Bao 1991; Mangalam & Wiita 1993). Recent models also include the effect of aberration based on the observer in a local static frame (Pecháček et al. 2005), hinting at the necessity for a full general relativistic (GR) treatment in the disk–jet case. A model for the QPO and its timing properties, such as the quality factor, the break frequency inferred from the PSD shape for a GR thin disk, was presented in Mohan & Mangalam (2014). There is a necessity for a treatment of the emission source kinematics and light ray paths in curved spacetime as the inner jet is close to the black hole; also, GR effects on this emission have not been treated in earlier works. A preliminary study was presented in Mohan (2014) and Mangalam & Mohan (2015).

A schematic indicating the basic features of the wind in the context of the black hole system is shown in Figure 1. The geometry consists of three zones. In the region ($R_s < r < R_{ISCO}$) marked as Zone 1, the radiation pressure is dominant and drives the outflowing blobs, which are sourced from a hot corona (thermal temperature of ∼85 keV, e.g., Mohan & Mangalam 2014) with zero angular momentum (as the inflow toward the black hole would be on plunging orbits).
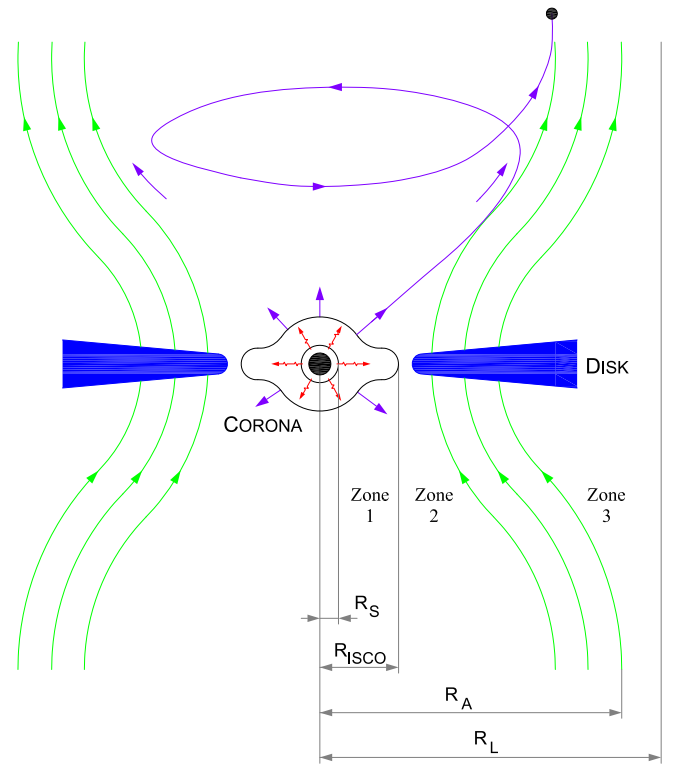
Figure 1. Schematic indicating the kinematically different zones in the trajectory of a typical blob. The black hole with a Schwarzschild radius $R_s = 2\,GM_\bullet/c^2$ is at the center. In the region ($R_s < r < R_{ISCO}$) marked Zone 1, radiation pressure is dominant and drives the outflowing blobs sourced from a zero angular momentum corona. In the transition region ($R_{ISCO} < r < R_A$) marked Zone 2, the kinematics of the flow are driven by radiation as well as the co-rotating magnetic field lines that are anchored to the disk. In Zone 3, at radii $R_A < r < R_L$, where R_A is the Alfvén radius and R_L is the radius of the light cylinder, the inertia dominates and the orbital angular momentum of the blob has reached an asymptotic value.

We consider the effects of radiation, namely pressure and drag in a two-dimensional model in Section 2, thereby extending the one-dimensional model of Abramowicz et al. (1990). In Section 3, we construct a model in Schwarzschild geometry for the kinematics and emission of the blob for the region ($R_A < r < R_L$) marked as Zone 3 and beyond ($r > R_L$). The transition region ($R_{ISCO} < r < R_A$) marked as Zone 2 requires a treatment of the relativistic Grad–Shafranov to self-consistently describe the geometry of the field and kinematics of the flow. While we postpone this for future studies, in this paper, we take the results from Section 2 to provide the launch parameters for calculating the blob trajectory in a conical or funnel geometry for the magnetized jet in Section 4. We assume that the blob that is accelerated by radiation reaches the magnetic surface where it is centrifugally driven to higher Lorentz factors by the co-rotation with the foot point. In the analysis in Section 4, applicable to Zone 3, we calculate the typical Lorentz factors that can be obtained both from the initial acceleration due to radiation in Zone 1 and the co-rotation in Zone 2; in Zone 3 we assume that the blob has reached a final angular momentum achieved at the Alfvén point; $j_\infty = \varpi_A^2 \Omega$ where ϖ_A is the cylindrical radius of the Alfvén point and Ω is the spin of the magnetic surface. Based on the kinematics of the model, the emission is also calculated for the centrifugally driven flow on an assumed conical- or funnel-

shaped geometry for the magnetic surface. While this is a simplified approach that improves upon previous work, we plan to construct a fully self-consistent model for Zone 2 in the future. We calculate the trajectory of the orbiting blob and the expected LC from a special relativistic cone model as presented in Camenzind & Krockenberger (1992) and then from a GR cone model and a realistic funnel model, given the instantaneous position and velocity in each case. Results from the analysis of simulated LCs include addressing the QPO phenomenon, its evolution and the shape of the power spectral density (PSD) for multiple emitting regions are presented in Section 4.4. We then discuss the advantages of our GR funnel model and interpret the results of the simulations in Section 5.

2. RADIATION-DRIVEN WIND IN THE LAUNCHING REGION

The effect of radiation pressure on radially outflowing relativistic particles has been studied by Abramowicz et al. (1990). While Vokrouhlicky & Karas (1991) included the black hole spin on the radiation pressure driven radial motion of particles, the effects of thermodynamic evolution was included by Horák & Karas (2006).

In addition to the effects of radiation pressure considered in Abramowicz et al. (1990), we extend their one-dimensional model to the general case of three dimensions (which simplifies to two for the resulting planar trajectories in a spherically symmetric metric) by including effects of radiation drag arising from the azimuthal and the θ components of the equations of motion. The four acceleration of the blobs in Schwarzschild geometry is set equal to the radiation forces of pressure and drag on the blob and hence the Lorentz factors are derived.

The observer geometry and the vectors are presented in Figure 3 of Abramowicz et al. (1990). First, we treat the blob motion in full (r, θ, ϕ) spherical coordinates. The evolution of the velocity due to the action of the radiation pressure and drag self-consistently governs the trajectory of the blobs until it reaches the launch positions on the magnetic surface at larger distances. The region where this occurs is radiation dominated and consists of a zero angular momentum hot flow sourced from a corona. The kinematics of this region, Zone 1, is of interest in the current section.

The model is cast in a Schwarzschild spacetime with the line element,

$$ds^2 = -(1 - 2M/r)c^2 dt^2$$
$$+ \frac{dr^2}{(1 - 2M/r)} + r^2\left(d\theta^2 + \sin^2 \theta d\phi^2\right), \quad (1)$$

where (r, θ, ϕ) are the spherical polar coordinates and $M = GM_\bullet/c^2$ is the gravitational radius with $M_\bullet$ being the black hole mass. The covariant components of this diagonal metric, expressed in these coordinates are given by

$$g_{\alpha\beta} = \left(g_{tt}, g_{rr}, g_{\theta\theta}, g_{\phi\phi}\right)$$
$$= \left(-(1 - 2M/r), \frac{1}{1 - 2M/r}, r^2, r^2 \sin^2 \theta\right). \quad (2)$$

By writing the line element in the form

$$ds^2 = -c^2 dt^2 (1 - 2M/r)\left(1 - (1 - 2M/r)^{-2}\left(\frac{dr}{dt}\right)^2\right)$$
$$- r^2(1 - 2M/r)^{-1}\left(\frac{d\theta}{dt}\right)^2$$
$$- r^2 \sin^2 \theta (1 - 2M/r)^{-1}\left(\frac{d\phi}{dt}\right)^2, \quad (3)$$

we can write the blob three-velocity components as

$$\beta_r = (1 - 2M/r)^{-1}\frac{1}{c}\frac{dr}{dt}$$
$$\beta_\theta = (1 - 2M/r)^{-1/2}\frac{r}{c}\frac{d\theta}{dt}$$
$$\beta_\phi = (1 - 2M/r)^{-1/2}\frac{r \sin \theta}{c}\frac{d\phi}{dt}. \quad (4)$$

With the above representation, the proper time $d\tau^2 = -ds^2$ can be written as

$$d\tau^2 = c^2 dt^2 \gamma^{-2}(1 - 2M/r), \quad (5)$$

where $\gamma = (1 - \beta_r^2 - \beta_\theta^2 - \beta_\phi^2)^{-1/2}$ is the Lorentz factor. The components of the four-velocity of the emitting blob along the jet $u^\alpha = dx^\alpha/d\tau = (dx^\alpha/dt)(dt/d\tau)$ are then

$$u^\alpha = \left(\frac{1}{c}(1 - 2M/r)^{-1/2}\gamma,\right.$$
$$(1 - 2M/r)^{1/2}\beta_r\gamma,$$
$$\left.\frac{1}{r}\beta_\theta\gamma, \frac{1}{r \sin \theta}\beta_\phi\gamma\right). \quad (6)$$

The covariant components of the four-velocity can be obtained by lowering the indices using the metric $u_\beta = u^\alpha g_{\alpha\beta}$,

$$u_\beta = \left(-(1 - 2M/r)^{1/2}\gamma,\right.$$
$$\left.\times (1 - 2M/r)^{-1/2}\beta_r\gamma, r\beta_\theta\gamma, r \sin \theta\beta_\phi\gamma\right). \quad (7)$$

The contra-variant components of the acceleration are given by

$$a^\alpha = \frac{du^\alpha}{d\tau} + \Gamma^\alpha_{\mu\nu}u^\mu u^\nu. \quad (8)$$

The radial component is then given by

$$a^r = \frac{\partial u^r}{\partial r}u^r + \frac{\partial u^r}{\partial \theta}u^\theta + \frac{\partial u^r}{\partial \phi}u^\phi + \Gamma^r_{\mu\nu}u^\mu u^\nu$$
$$= \frac{\partial u^r}{\partial r}u^r + \frac{\partial u^r}{\partial \theta}u^\theta + \frac{\partial u^r}{\partial \phi}u^\phi + \Gamma^r_{tt}\left(u^t\right)^2$$
$$+ \Gamma^r_{rr}\left(u^r\right)^2 + \Gamma^r_{\phi\phi}\left(u^\phi\right)^2. \quad (9)$$

Using the four-velocity components from Equation (6) and $\Gamma^r_{tt} = \frac{M}{r^2}(1 - 2M/r)$, $\Gamma^r_{rr} = \frac{M}{r^2}(1 - 2M/r)^{-1}$,

$$\Gamma^r_{\phi\phi} = -r \, \sin^2 \, \theta (1 - 2M/r),$$

$$a^r = \gamma^2 \left[\frac{M}{r^2} + \beta_r (1 - 2M/r)\left(1 + \beta_r^2 \gamma^2\right)\frac{\partial \beta_r}{\partial r} \right.$$

$$+ \beta_r^2 \gamma^2 (1 - 2M/r)\left(\beta_\theta \frac{\partial \beta_\theta}{\partial r} + \beta_\phi \frac{\partial \beta_\phi}{\partial r}\right)$$

$$- \frac{M}{r}(1 - 2M/r)\left(\beta_\theta^2 + \beta_\phi^2\right) + \frac{\beta_\theta (1 - 2M/r)^{1/2}}{r}$$

$$\times \left\{ \left(1 + \beta_r^2 \gamma^2\right)\frac{\partial \beta_r}{\partial \theta} + \beta_r \gamma^2 \left(\beta_\theta \frac{\partial \beta_\theta}{\partial \theta} + \beta_\phi \frac{\partial \beta_\phi}{\partial \theta}\right)\right\}$$

$$+ \frac{\beta_\phi (1 - 2M/r)^{1/2}}{r \, \sin \theta}\left\{ \left(1 + \beta_r^2 \gamma^2\right)\frac{\partial \beta_r}{\partial \phi} \right.$$

$$\left. \left. + \beta_r \gamma^2 \left(\beta_\theta \frac{\partial \beta_\theta}{\partial \phi} + \beta_\phi \frac{\partial \beta_\phi}{\partial \phi}\right)\right\}\right] \tag{10}$$

The quantity $mc^2 a^r$ is the radial force where m is the mass of the orbiting blob. The θ-component of the acceleration is given by

$$a^\theta = \frac{\partial u^\theta}{\partial r}u^r + \frac{\partial u^\theta}{\partial \theta}u^\theta + \frac{\partial u^\theta}{\partial \phi}u^\phi + \Gamma^\theta_{\mu\nu}u^\mu u^\nu$$

$$= \frac{\partial u^\theta}{\partial r}u^r + \frac{\partial u^\theta}{\partial \theta}u^\theta + \frac{\partial u^\theta}{\partial \phi}u^\phi + \Gamma^\theta_{\phi\phi}\left(u^\phi\right)^2$$

$$+ 2\Gamma^\theta_{r\theta}u^r u^\theta. \tag{11}$$

Using the four-velocity components from Equation (6), $\Gamma^\theta_{\phi\phi} = -\cos \theta \, \sin \theta$ and $\Gamma^\theta_{r\theta} = 1/r$,

$$a^\theta = \frac{\gamma^2}{r}\left[\beta_r (1 - 2M/r)^{1/2}\left\{ \left(1 + \beta_\theta^2 \gamma^2\right)\frac{\partial \beta_\theta}{\partial r} \right.\right.$$

$$+ \beta_\theta \gamma^2 \left(\beta_r \frac{\partial \beta_r}{\partial r} + \beta_\phi \frac{\partial \beta_\phi}{\partial r}\right) + \frac{\beta_\theta}{r}\Big\}$$

$$+ \frac{\beta_\theta}{r}\left\{ \left(1 + \beta_\theta^2 \gamma^2\right)\frac{\partial \beta_\theta}{\partial \theta} + \beta_\theta \gamma^2 \left(\beta_r \frac{\partial \beta_r}{\partial \theta} + \beta_\phi \frac{\partial \beta_\phi}{\partial \theta}\right)\right\}$$

$$+ \frac{\beta_\phi}{r \, \sin \theta}\left\{ \left(1 + \beta_\theta^2 \gamma^2\right)\frac{\partial \beta_\theta}{\partial \phi} \right.$$

$$\left. \left. + \beta_\theta \gamma^2 \left(\beta_r \frac{\partial \beta_r}{\partial \phi} + \beta_\phi \frac{\partial \beta_\phi}{\partial \phi}\right)\right\} - \frac{\cot \, \theta}{r}\beta_\phi^2 \right] \tag{12}$$

The quantity $mc^2 r a^\theta$ is the force in the θ direction. The azimuthal component is given by

$$a^\phi = \frac{\partial u^\phi}{\partial r}u^r + \frac{\partial u^\phi}{\partial \theta}u^\theta + \frac{\partial u^\phi}{\partial \phi}u^\phi + \Gamma^\phi_{\mu\nu}u^\mu u^\nu$$

$$= \frac{\partial u^\phi}{\partial r}u^r + \frac{\partial u^\phi}{\partial \theta}u^\theta + \frac{\partial u^\phi}{\partial \phi}u^\phi + 2\Gamma^\phi_{r\phi}u^r u^\phi$$

$$+ 2\Gamma^\phi_{\theta\phi}u^\theta u^\phi. \tag{13}$$

Using the four-velocity components from Equation (6), $\Gamma^\phi_{r\phi} = 1/r$ and $\Gamma^\phi_{\theta\phi} = \cot \, \theta$,

$$a^\phi = \frac{\gamma^2}{r \, \sin \theta}\left[\beta_r (1 - 2M/r)^{1/2}\left\{ \left(1 + \beta_\phi^2 \gamma^2\right)\frac{\partial \beta_\phi}{\partial r} \right.\right.$$

$$+ \beta_\phi \left(\frac{M}{r} - \cot \, \theta \frac{\partial \beta_\theta}{\partial r} + \gamma^2 \left(\beta_r \frac{\partial \beta_r}{\partial r} + \beta_\theta \frac{\partial \beta_\theta}{\partial r}\right)\right)\Big\}$$

$$+ \frac{\beta_\theta}{r}\left\{ \left(1 + \beta_\phi^2 \gamma^2\right)\frac{\partial \beta_\phi}{\partial \theta} + 2\beta_\phi \, \cot \, \theta \right.$$

$$\left. + \beta_\phi \gamma^2 \left(\beta_r \frac{\partial \beta_r}{\partial \theta} + \beta_\theta \frac{\partial \beta_\theta}{\partial \theta}\right)\right\}$$

$$+ \frac{\beta_\phi}{r \, \sin \theta}\left\{ \left(1 + \beta_\phi^2 \gamma^2\right)\frac{\partial \beta_\phi}{\partial \phi} \right.$$

$$\left. \left. + \beta_\phi \gamma^2 \left(\beta_r \frac{\partial \beta_r}{\partial \phi} + \beta_\theta \frac{\partial \beta_\theta}{\partial \phi}\right)\right\}\right]. \tag{14}$$

The quantity $mc^2 r a^\phi$ represents the force in the azimuthal direction. Radiation force drives the accelerated outward motion of the blob while the initial azimuthal and angular motion, however, is continuously retarded by the effect of the radiation drag of an assumed spherically symmetric radiation field.

Following Abramowicz et al. (1990), the contra-variant components of the radiation energy flux are given by

$$F^\alpha = h^\alpha_\mu T^{\mu\nu}u_\nu, \tag{15}$$

where $h^\alpha_\mu = \delta^\alpha_\mu + u^\alpha u_\mu$ is a projection tensor and $T^{\mu\nu}$ is the radiation field energy density. The tetrad components of the energy density tensor can be evaluated using

$$T^{(i)(k)} = \int I(r)n^{(i)}n^{(k)}d\Omega \tag{16}$$

where $I(r)$ is the radiation field intensity, $n^{(i)}$ is the unit vector describing the photon trajectory, and $d\Omega$ is an element of the solid angle subtended on the sky of the local observer (see Figure 3 of Abramowicz et al. 1990). The energy density can thus be evaluated from this using

$$T^{tt} = T^{(t)(t)}(1 - 2M/r)^{-1}$$

$$= 2\pi I(r)(1 - 2M/r)^{-1}(1 - \cos \eta)$$

$$T^{tr} = T^{rt} = T^{(t)(r)} = T^{(r)(t)} = \pi I(r)\sin^2 \, \eta$$

$$T^{rr} = T^{(r)(r)}(1 - 2M/r) = \frac{2\pi I(r)}{3}$$

$$\times (1 - 2M/r)\left(1 - \cos^3 \, \eta\right)$$

$$T^{\theta\theta} = \frac{T^{(\theta)(\theta)}}{r^2} = \frac{\pi I(r)}{3r^2}\left(\cos^3 \, \eta - 3 \cos \eta + 2\right)$$

$$T^{\phi\phi} = \frac{T^{(\phi)(\phi)}}{r^2 \, \sin^2 \, \theta} = \frac{\pi I(r)}{3r^2 \, \sin^2 \, \theta}\left(\cos^3 \, \eta - 3 \cos \eta + 2\right), \tag{17}$$

where $R = 6M$ is the radius of the emitting surface, η is the viewing angle from the zenith for the stationary observer and is

related to δ, which is the zenithal angle at the point of emission, R, by

$$\sin \eta = \frac{M}{r} \frac{(1 - 2M/r)^{1/2}}{(1 - 2M/R)^{1/2}} \sin \delta, \qquad (18)$$

where $\sin \delta = 1$ for $R/M > 3/2$ and $\sin \delta = \frac{3\sqrt{3}}{2} \frac{M}{R} (1 - 2M/R)^{1/2}$ for $R/M \leqslant 3/2$ (Abramowicz et al. 1990).

If σ is the cross section of the orbiting blob over which the radiation force acts, the quantity σF^α represents the radiation force. The radial component of the energy flux is given by

$$F^r = \Big[\big(1 + u^r u_r\big)\big(T^{rt} u_t + T^{rr} u_r\big) + u^r u_t \big(T^{tt} u_t + T^{tr} u_r\big)$$
$$+ u^r u_\theta \big(T^{\theta\theta} u_\theta\big) + u^r u_\phi \big(T^{\phi\phi} u_\phi\big) \Big]. \qquad (19)$$

Using the components of u^α from Equation (6), u_α from Equation (7), and $T^{\mu\nu}$ from Equation (17), the radiation force in the radial direction is given by

$$\sigma F^r = \pi I(r)\sigma\gamma^3 (1 - 2M/r)^{1/2}$$
$$\times \Bigg[\frac{1 + \beta_r^2 \gamma^2}{\gamma^2} \Big(-\sin^2 \eta + \frac{2}{3}\beta_r\big(1 - \cos^3 \eta\big) \Big)$$
$$- \beta_r \big(\beta_r \sin^2 \eta - 2(1 - \cos \eta) \big)$$
$$+ \frac{\beta_r}{3}\big(\beta_\theta^2 + \beta_\phi^2\big)\big(\cos^3 \eta - 3\cos \eta + 2\big) \Bigg]. \qquad (20)$$

The θ-component of the energy flux is given by

$$F^\theta = \big(1 + u^\theta u_\theta\big)T^{\theta\theta} u_\theta + u^\theta u_t \big(T^{tt} u_t + T^{tr} u_r\big)$$
$$+ u^\theta u_r \big(T^{rt} u_t + T^{rr} u_r\big) + u^\theta u_\phi \big(T^{\phi\phi} u_\phi\big). \qquad (21)$$

Using the components of u^α from Equation (6), u_α from Equation (7) and the components of $T^{\mu\nu}$ from Equation (17), the θ-component of the radiation force is given by

$$\sigma F^\theta = \frac{\pi I(r)\sigma\gamma^3 \beta_\theta}{r} \Bigg[\frac{1 + \beta_\theta^2 \gamma^2}{3\gamma^2} \big(\cos^3 \eta - 3\cos \eta + 2 \big)$$
$$+ 2(1 - \cos \eta) - \frac{2}{3}\beta_r^2 \big(1 - \cos^3 \eta\big)$$
$$+ \beta_\theta^2 \big(\cos^3 \eta - 3\cos \eta + 2 \big) \Bigg]. \qquad (22)$$

The azimuthal component of the energy flux is given by

$$F^\phi = \Big[\big(1 + u^\phi u_\phi\big)T^{\phi\phi} u_\phi + u^\phi u_t \big(T^{tt} u_t + T^{tr} u_r\big)$$
$$+ u^\phi u_r \big(T^{rt} u_t + T^{rr} u_r\big) + u^\phi u_\theta T^{\theta\theta} u_\theta \Big]. \qquad (23)$$

Using the components of u^α from Equation (6), u_α from Equation (7), and the components of $T^{\mu\nu}$ from Equation (17),

the azimuthal component of the radiation force is given by

$$\sigma F^\phi = \frac{\pi I(r)\sigma\gamma^3 \beta_\phi}{r \, \sin \theta} \Bigg[\frac{1 + \beta_\phi^2 \gamma^2}{3\gamma^2} \big(\cos^3 \eta - 3\cos \eta + 2 \big)$$
$$+ 2(1 - \cos \eta) - \frac{2}{3}\beta_r^2 \big(1 - \cos^3 \eta\big)$$
$$+ \beta_\theta^2 \big(\cos^3 \eta - 3\cos \eta + 2 \big) \Bigg]. \qquad (24)$$

2.1. Dynamics Based on Radiation Pressure and Drag

The Eddington parameter Γ_ϵ is the ratio of the disk luminosity L to the Eddington luminosity L_{Edd} and is given by,

$$\Gamma_\epsilon = \frac{L}{L_{\mathrm{Edd}}} = \frac{c\pi I(R)\sigma R^2 (1 - 2M/R)^{1/2}}{GM_\bullet mc} \qquad (25)$$

where L_{Edd} is corrected for the GR redshift factor $(1 - 2M/R)^{1/2}$ and σ is the cross section of the orbiting blob over which the radiation force acts and

$$\frac{I(r)}{I(R)} = \left(\frac{1 - 2M/R}{1 - 2M/r} \right)^2, \qquad (26)$$

is obtained from the energy conservation along the null trajectory in the stationary frame (Abramowicz et al. 1990).

The first equation of motion is from the radial components of the acceleration and the force. The radial component of the force imparts the radial acceleration onto the orbiting blob, i.e., $\sigma F^r = mc^2 a^r$. Using Equations (10) and (20) and the representation $x = r/M$ and $X = R/M$, we can eliminate the dependence of the equation on M. Then, expressing the equation in terms of the Eddington parameter Γ_ϵ using Equations (25) and (26),

$$\frac{1}{x^2} + \beta_r(1 - 2/x)\big(1 + \beta_r^2 \gamma^2\big)\frac{\partial \beta_r}{\partial x}$$
$$+ \beta_r^2 \gamma^2 (1 - 2/x)\bigg(\beta_\theta \frac{\partial \beta_\theta}{\partial x} + \beta_\phi \frac{\partial \beta_\phi}{\partial x} \bigg)$$
$$- \frac{1}{x}(1 - 2/x)\big(\beta_\theta^2 + \beta_\phi^2\big) + \frac{\beta_\theta (1 - 2/x)^{1/2}}{x}$$
$$\times \bigg\{ \big(1 + \beta_r^2 \gamma^2\big)\frac{\partial \beta_r}{\partial \theta} + \beta_r \gamma^2 \bigg(\beta_\theta \frac{\partial \beta_\theta}{\partial \theta} + \beta_\phi \frac{\partial \beta_\phi}{\partial \theta} \bigg) \bigg\}$$
$$+ \frac{\beta_\phi (1 - 2/x)^{1/2}}{x \sin \theta} \bigg\{ \big(1 + \beta_r^2 \gamma^2\big)\frac{\partial \beta_r}{\partial \phi}$$
$$+ \beta_r \gamma^2 \bigg(\beta_\theta \frac{\partial \beta_\theta}{\partial \phi} + \beta_\phi \frac{\partial \beta_\phi}{\partial \phi} \bigg) \bigg\}$$
$$= \frac{\Gamma_\epsilon \gamma}{X^2} \bigg(\frac{1 - 2/X}{1 - 2/x} \bigg)^{3/2} \Bigg[\frac{1 + \beta_r^2 \gamma^2}{\gamma^2} \big(-\sin^2 \eta$$
$$+ \frac{2}{3}\beta_r\big(1 - \cos^3 \eta\big) \big)$$
$$- \beta_r \big(\beta_r \sin^2 \eta - 2(1 - \cos \eta)$$
$$+ \frac{\beta_\theta^2 + \beta_\phi^2}{3} \big(\cos^3 \eta - 3\cos \eta + 2 \big) \Bigg]. \qquad (27)$$

The second equation of motion is from the θ-components of the acceleration and the force. The θ-component of the force imparts a drag on the acceleration of the orbiting blob and $\sigma F^\theta = mc^2 a^\theta$. Using $\gamma_r = (1 - \beta_r^2)^{1/2}$, Equations (12) and (22) and the representation $x = r/M$ and $X = R/M$, and expressing the equation in terms of the Eddington parameter Γ_ϵ using Equations (25) and (26),

$$\beta_r (1 - 2/x)^{1/2} \left\{ \left(1 + \beta_\theta^2 \gamma^2\right) \frac{\partial \beta_\theta}{\partial x} + \beta_\theta \gamma^2 \left(\beta_r \frac{\partial \beta_r}{\partial x} + \beta_\phi \frac{\partial \beta_\phi}{\partial x} \right) + \frac{\beta_\theta}{x} \right\}$$

$$+ \frac{\beta_\theta}{x} \left\{ \left(1 + \beta_\theta^2 \gamma^2\right) \frac{\partial \beta_\theta}{\partial \theta} + \beta_\theta \gamma^2 \left(\beta_r \frac{\partial \beta_r}{\partial \theta} + \beta_\phi \frac{\partial \beta_\phi}{\partial \theta} \right) \right\}$$

$$+ \frac{\beta_\phi}{x \sin \theta} \left\{ \left(1 + \beta_\theta^2 \gamma^2\right) \frac{\partial \beta_\theta}{\partial \phi} + \beta_\theta \gamma^2 \left(\beta_r \frac{\partial \beta_r}{\partial \phi} + \beta_\phi \frac{\partial \beta_\phi}{\partial \phi} \right) \right\}$$

$$- \frac{\cot \theta}{x} \beta_\phi^2 = \frac{\Gamma_\epsilon \gamma \beta_\theta}{X^2 (1 - 2/X)^{1/2}} \left(\frac{1 - 2/X}{1 - 2/x} \right)^2$$

$$\times \left[2(1 - \cos \eta) - \frac{2}{3} \beta_r^2 \left(1 - \cos^3 \eta\right) \right.$$

$$\left. + \frac{1}{3} \left(\frac{1}{\gamma_r^2} + 2\beta_\phi^2 \right) \left(\cos^3 \eta - 3\cos \eta + 2\right) \right]. \tag{28}$$

The third equation of motion is from the azimuthal components of the acceleration and the force. The azimuthal component of the force imparts a drag on the azimuthal acceleration of the orbiting blob and $\sigma F^\phi = mc^2 a^\phi$. Using Equations (14) and (24) and the representation $x = r/M$ and $X = R/M$, and expressing the equation in terms of the Eddington parameter Γ_ϵ, using Equations (25) and (26),

$$\beta_r (1 - 2/x)^{1/2} \left\{ \left(1 + \beta_\phi^2 \gamma^2\right) \frac{\partial \beta_\phi}{\partial x} + \beta_\phi \left(\frac{1}{x} - \cot \theta \frac{\partial \beta_\theta}{\partial x} \right. \right.$$

$$\left. \left. + \gamma^2 \left(\beta_r \frac{\partial \beta_r}{\partial x} + \beta_\theta \frac{\partial \beta_\theta}{\partial x} \right) \right) \right\}$$

$$+ \frac{\beta_\theta}{x} \left\{ \left(1 + \beta_\phi^2 \gamma^2\right) \frac{\partial \beta_\phi}{\partial \theta} + 2\beta_\phi \cot \theta \right.$$

$$\left. + \beta_\phi \gamma^2 \left(\beta_r \frac{\partial \beta_r}{\partial \theta} + \beta_\theta \frac{\partial \beta_\theta}{\partial \theta} \right) \right\} + \frac{\beta_\phi}{x \sin \theta} \left\{ \left(1 + \beta_\phi^2 \gamma^2\right) \frac{\partial \beta_\phi}{\partial \phi} \right.$$

$$\left. + \beta_\phi \gamma^2 \left(\beta_r \frac{\partial \beta_r}{\partial \phi} + \beta_\theta \frac{\partial \beta_\theta}{\partial \phi} \right) \right\}$$

$$= \frac{\Gamma_\epsilon \gamma \beta_\phi}{X^2 (1 - 2/X)^{1/2}} \left(\frac{1 - 2/X}{1 - 2/x} \right)^2$$

$$\times \left[2(1 - \cos \eta) - \frac{2}{3} \beta_r^2 \left(1 - \cos^3 \eta\right) \right.$$

$$\left. + \frac{1}{3} \left(\frac{1}{\gamma_r^2} + 2\beta_\theta^2 \right) \left(\cos^3 \eta - 3\cos \eta + 2\right) \right]. \tag{29}$$

2.1.1. Purely Radial Motion

In the limits $\beta_\phi = 0$ and $\beta_\theta = 0$, i.e., purely radial outflowing motion, only the first equation of motion is

relevant. The equation reduces to

$$(1 - 2/x)\gamma_r^2 \beta_r \frac{d\beta_r}{dx} + \frac{1}{x^2} = \frac{\Gamma_\epsilon}{x^2} \left(\frac{1 - 2/X}{1 - 2/x} \right)^{3/2}$$

$$\times \left[-\sin^2 \eta \left(1 + \beta_r^2\right) + \frac{2}{3} \beta_r \left(4 - \cos^3 \eta - 3\cos \eta\right) \right], \tag{30}$$

which is the same as that derived in Abramowicz et al. (1990). Solving for β_r and hence $\gamma_r = (1 - \beta_r^2)^{-1/2}$ as a function of the initial launch velocity, $\beta_{r,i}$ and x indicates a constant saturation value of 2–7 for $\Gamma_\epsilon = 0.3$, $\beta_{r,i} = 0.86$–0.99 at distances r beyond ~a few tens of M from the black hole and is plotted in Figure 2. In the simulations, changes to Γ_ϵ did not change these results.

For the range of $\beta_{r,i} = 0.86-0.99$ and $x = 6-20$, the γ_r contours saturate at constant values in the range 2−7 for large x, consistent with the simulations of Abramowicz et al. (1990).
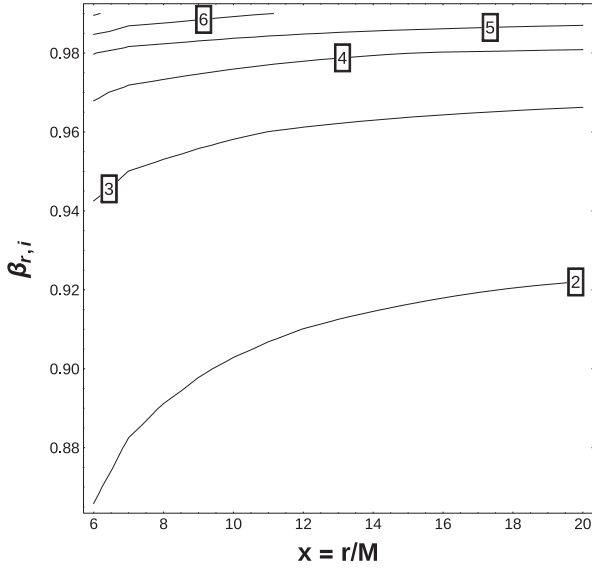
2.1.2. Poloidal Motion

A poloidal outflow in the radiation region ($\beta_\phi = 0$, $\beta_\theta \neq 0$, $\beta_r \neq 0$) is trajectorially equivalent to the case of motion on the equatorial plane ($\theta = \pi/2$, $\beta_\theta = 0$, $\beta_\phi \neq 0$, $\beta_r \neq 0$) due to the spherical symmetry of the Schwarzschild geometry. We appeal to the zero angular momentum nature of the outflow source in the corona region (see Figure 1) to motivate this poloidal flow. Thus, we are left with two coupled partial differential equations to solve modified versions of Equations (27) and (28) with ($\beta_\phi = 0$, $\beta_\theta \neq 0$, $\beta_r \neq 0$). The bulk Lorentz factor $\gamma = (1 - \beta_r^2 - \beta_\theta^2)^{-1/2}$ in this case and $\gamma_r = (1 - \beta_r^2)^{-1/2}$; $\gamma_\theta = (1 - \beta_\theta^2)^{-1/2}$. The resulting equations are,

$$\frac{1}{x^2} + \beta_r \gamma^2 (1 - 2/x) \left(\frac{1}{\gamma_\theta^2} \frac{\partial \beta_r}{\partial x} + \beta_r \beta_\theta \frac{\partial \beta_\theta}{\partial x} \right) - \frac{\beta_\theta^2}{x}(1 - 2/x)$$

$$+ \frac{\beta_\theta \gamma^2}{x}(1 - 2/x)^{1/2} \left(\frac{1}{\gamma_\theta^2} \frac{\partial \beta_r}{\partial \theta} + \beta_r \beta_\theta \frac{\partial \beta_\theta}{\partial \theta} \right)$$

$$= \frac{\Gamma_\epsilon \gamma}{X^2} \left(\frac{1 - 2/X}{1 - 2/x} \right)^{3/2} \left[\frac{1}{\gamma_\theta^2} \left(-\sin^2 \eta + \frac{2}{3} \beta_r \left(1 - \cos^3 \eta\right) \right) \right.$$

$$- \beta_r \left(\beta_r \sin^2 \eta - 2(1 - \cos \eta) \right.$$

$$\left. \left. + \frac{\beta_\theta^2}{3} \left(\cos^3 \eta - 3\cos \eta + 2\right) \right) \right], \tag{31}$$

for the radial motion, and the θ-equation is

$$\beta_r (1 - 2/x)^{1/2} \left(\frac{\gamma^2}{\gamma_r^2} \frac{\partial \beta_\theta}{\partial x} + \beta_\theta \beta_r \gamma^2 \frac{\partial \beta_r}{\partial x} + \frac{\beta_\theta}{x} \right)$$

$$+ \frac{\beta_\theta \gamma^2}{x} \left(\frac{1}{\gamma_r^2} \frac{\partial \beta_\theta}{\partial \theta} + \beta_\theta \beta_r \frac{\partial \beta_r}{\partial \theta} \right)$$

Figure 2. Contours of γ_r as a function of the initial launch velocity $\beta_{r,i}$ and x. The γ_r value tapers off to constant values at large x for $\beta_{r,i} = 0.86-0.99$ consistent with the simulations performed in Abramowicz et al. (1990). The simulated γ_r are in the range 2–7.

$$= \frac{\Gamma_\epsilon \gamma \beta_\theta}{X^2 (1 - 2/X)^{1/2}} \left(\frac{1 - 2/X}{1 - 2/x} \right)^2 \left[2(1 - \cos \eta) \right.$$
$$- \frac{2}{3}\beta_r^2 \left(1 - \cos^3 \eta \right)$$
$$\left. + \frac{1}{3\gamma_r^2} \left(\cos^3 \eta - 3\cos \eta + 2 \right) \right]. \qquad (32)$$

In the simulations carried out, we set $\Gamma_\epsilon = 0.3$. The initial value $\beta_{r,i}$ was varied between 0.01 and 0.99, the range being chosen based on the β_r range simulated in Mohan & Mangalam (2014) for a relativistic thin disk (Novikov & Thorne 1973; Shakura & Sunyaev 1973) in the context of the quality factor Q observable in the inner region of the accretion disk very close to the ISCO. There, we obtained the range $1.36 \times 10^5 - 0.99$ for a range of the disk viscosity parameter $\alpha = 0.01-0.4$ for $r \geqslant 6\,M-20M$. The range of initial velocity $\beta_{\theta,i}$ is chosen based on the argument that if the motion is along Keplerian orbits, $\beta_\theta = (1-2M/r)^{-1/2} \frac{r}{c} \frac{d\theta}{dt} = (1-2M/r)^{-1/2} \frac{r}{c} \Omega(r)$. As $\Omega(r) = c(M/r^3)^{1/2}$ for Keplerian orbits, $\beta_\theta = (1-2M/r)^{-1/2}(M/r)^{1/2}$. We thus evaluate $\beta_{\theta,i}$ to be in the range $0.25-0.61$ for $r = 6\,M-20M$.

The initial values $\beta_{r,i}$ and $\beta_{\theta,i}$ were taken in the range 0.86–0.99 (similar to the case of purely radial flow) and 0.25–0.61, respectively. The initial values of the variables x and θ were taken in the range 6–20 and $0.01 - \pi/2$, respectively. The contours of β_θ and $\gamma = (1 - \beta^2)^{-1/2}$, where $\beta = (\beta_r^2 + \beta_\theta^2)^{1/2}$ as a function of x and θ, are plotted in Figure 3. Simulated final values of β_θ are in the range 0.18–0.81 and γ are in the range 1.1–26.3, higher than in the purely radial case though, γ saturates to low values for smaller initial values of x. It is inferred from the simulations that β_θ and γ decrease rapidly; this decrease is large for smaller initial values of x, while their decrease is more gradual at larger initial

values of x. These effects can be attributed to the drag force due to the non-radial component of the radiation pressure, which plays an important role in stabilizing the saturation values of γ at an early stage even if the source of the outflow had an initial angular momentum. The simulations thus indicate that the flow becomes rapidly radial.

We plan to present details of the classification of flows, and hence a more comprehensive exploration of the parameter space and the resulting trajectories in a paper in preparation. Here, we have derived the typical values of the poloidal β_p and γ_p that are the inputs to typical initial values for Zone 3 $(R_A < r < R_L)$ and beyond $(r > R_L)$ where the angular momentum is set by its value at the Alfvén point.

3. TRAJECTORY AND EMISSION GEOMETRY IN AND BEYOND ZONE 3

From the metric in Equation (1), there is no explicit dependence in the equations of motion on the ϕ and t coordinates, there are two Killing vectors associated with this geometry given by $\zeta = (1, 0, 0, 0)$ and $\eta = (0, 0, 0, 1)$. If u is the four-velocity of the emitting blob, the Killing vectors can be used to evaluate the constants of motion for the Schwarzschild metric including the the total energy

$$\varepsilon = -\zeta \cdot \mathbf{u} = \frac{u^t}{(1 - 2M/R)}, \qquad (33)$$

and the conserved angular momentum

$$j = -\eta \cdot \mathbf{u} = \Omega R^2 \sin^2 \theta, \qquad (34)$$

where u^t is the time component of the four velocity u and Ω is the angular velocity of Keplerian orbits in Schwarzschild geometry. The condition $\mathbf{u \cdot u} = -1$ in case of the Schwarzschild metric gives

$$u^t = \gamma_{\text{jet}} = \left(1 - 2M/R - \frac{\dot{R}^2/c^2}{1 - 2M/R} \right.$$
$$\left. - R^2 \dot{\theta}^2/c^2 - R^2 \sin^2 \theta \, \dot{\phi}^2/c^2 \right)^{-1/2}. \qquad (35)$$

This can be used to write the general expression for the velocity β_{jet} of the emitting spot as

$$\beta_{\text{jet}} = \frac{\dot{R}^2/c^2}{1 - 2M/R} - R^2 \dot{\theta}^2/c^2 - R^2 \sin^2 \theta \, \dot{\phi}^2/c^2$$
$$= \left(1 - 2M/R - 1/\gamma_{\text{jet}}^2 \right)^{1/2} \qquad (36)$$

The various emission and direction vectors include the radial vector $\mathbf{n}$, the direction vector of the initially emitted light ray $\mathbf{k_0}$ and the final direction vector pointing along the observer line of sight $\mathbf{k}$. A general path showing the source motion along a helical trajectory and the emission geometry along with the above vectors is presented in a schematic in Figure 4.

The vector $\mathbf{k_0}$ is given in terms of $\mathbf{k}$ and $\mathbf{n}$ as

$$\mathbf{k_0} = \frac{\sin \alpha}{\sin \psi} \mathbf{k} + \frac{\sin(\psi - \alpha)}{\sin \psi} \mathbf{n}; \qquad (37)$$

this identity can be verified applying dot and cross products of $\mathbf{k}$ and $\mathbf{n}$ and using their geometry given in Figure 4.
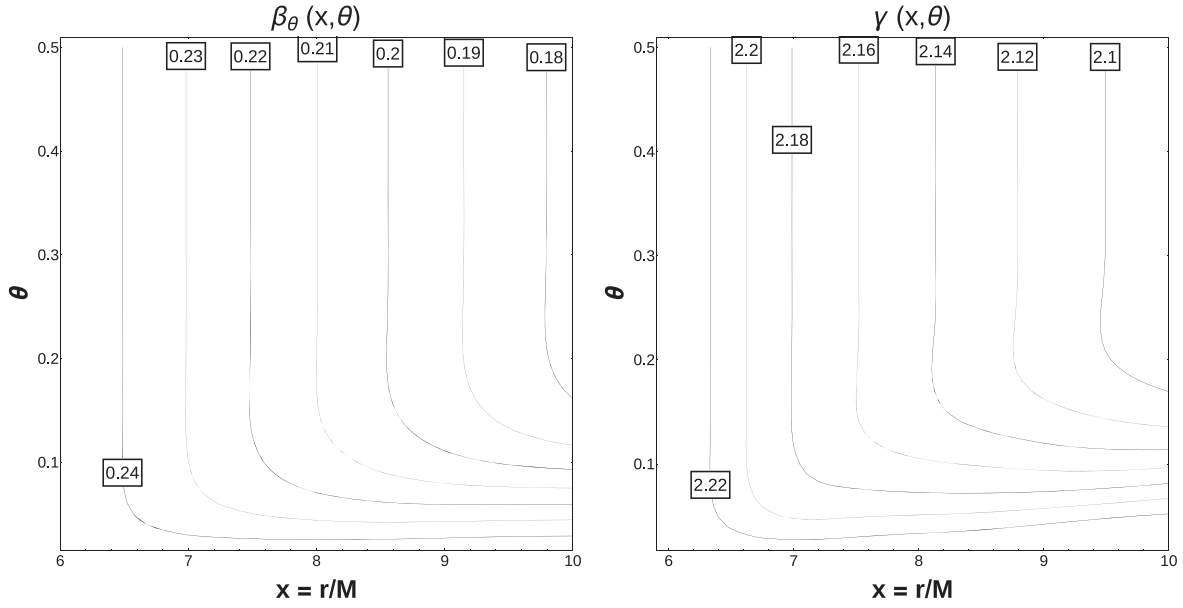
Figure 3. Contour plots of $\beta_\theta(x, \theta)$ and $\gamma(x, \theta) = (1 - \beta^2)^{-1/2}$ where $\beta = (\beta_r^2 + \beta_\theta^2)^{1/2}$ for $\beta_{r,i} = 0.86-0.99$ and $\beta_{\theta,i} = 0.25-0.61$. Left plot: simulated β_θ is in the range 0.18–0.81. The decrease in β_θ are large for smaller initial values of x. Right plot: the decrease in γ also follows the same expected trend to that of β_θ. The simulated γ are in the range 1.1–26.3, higher than in the purely radial case, though, with saturation of γ to low values occurring even at smaller x. These effects can be attributed to the drag force acting to rapidly cause the loss of any initial angular momentum as well as stabilize the flow at small x.

In the Cartesian (x, y, z) coordinate system centered on the black hole, the components of the direction vector $\mathbf{k}$ are given by

$$\mathbf{k} = (\sin i, \, 0, \, \cos i) \tag{38}$$

and the components of the emission vector $\boldsymbol{n}$ are given by

$$\mathbf{n} = (\sin\theta\cos\phi, \, \sin\theta\sin\phi, \, \cos\theta). \tag{39}$$

The initial emission angle α can be written in terms of the initial direction vector $\mathbf{k_0}$ and the emission vector $\mathbf{n}$ as $\cos\alpha = \mathbf{k_0} \cdot \mathbf{n}$. The final angle of the emitted ray ψ can be written in terms of the final direction vector $\boldsymbol{k}$ and the emission vector $\boldsymbol{n}$ as $\cos\psi = \mathbf{k} \cdot \mathbf{n}$. This can be expanded as

$$\cos\psi = \cos i \cos\theta + \sin i \, \sin\theta\cos\phi. \tag{40}$$

Assume that an emitter located at a radial distance R emits a light ray at an angle α with respect to the radial vector. The light ray undergoes bending due to spacetime curvature to emerge at a final angle ψ with respect to the radial vector and the relationship between ψ and α can be determined by solving and combining

$$\psi = \int_R^\infty \frac{dr}{r^2}\left(1/b^2 - 1/r^2(1 - 2M/r)\right)^{-1/2} \tag{41}$$

and

$$\sin\alpha = \frac{b}{R}(1 - 2M/R)^{1/2}, \tag{42}$$

where b is the impact parameter shown in Figure 4. The derivation of the above equation is presented in Appendix. This propagation effect can be approximated by the expression (Beloborodov 2002)

$$1 - \cos\alpha = (1 - \cos\psi)(1 - 2M/R). \tag{43}$$

Using the above approximation, we find

$$\frac{\sin\alpha}{\sin\psi} = (1 - 2M/R)^{1/2}(1 - 2M/R$$
$$+ (4\,M/R)(1 + \cos\psi)^{-1})^{1/2}. \tag{44}$$

The travel time will be different for photons emitted from different radial locations R. The difference between the travel time for a ray emitted from a position R and that from a position at the center of the coordinate system can be obtained from the integral

$$\Delta t$$
$$= \int_R^\infty \frac{dr}{1 - 2M/r}\left(\left(1 - \frac{b^2}{r^2}(1 - 2M/r)\right)^{-1/2} - 1\right). \tag{45}$$

The time delay due to light bending can be approximated (Poutanen & Beloborodov 2006) as

$$\Delta t_{\mathrm{LB}} = \left(\frac{\delta}{8}y^2\left(1 + y\left(\frac{1}{3} - \frac{2\delta}{14}\right)\right)\right)\frac{R}{c}, \tag{46}$$

where $y = (1 - \cos\psi)$ and $\delta = 2M/R$. The time delay is defined with respect to straight paths from point P to the observer, as shown in Figure 4.

The time of advance due to orbital motion of the emitting source, t_{adv}, can be expressed in terms of geometric factors from Figure 4 as

$$t_{\mathrm{adv}} = (1 - y)R/c - (\boldsymbol{n_{0\cdot i}})\varpi_0/c, \tag{47}$$

where the constant shift $(\boldsymbol{n_{0\cdot i}})$ accounts for the initial offset in R in the projected $\boldsymbol{i}$ direction toward the observer. If the time of emission in the source frame is t_{em}, the observed period of the signal t_{obs} is reduced due to the effects of the component of the source moving toward the observer's line of sight and due to the time delay induced by light bending and the disk
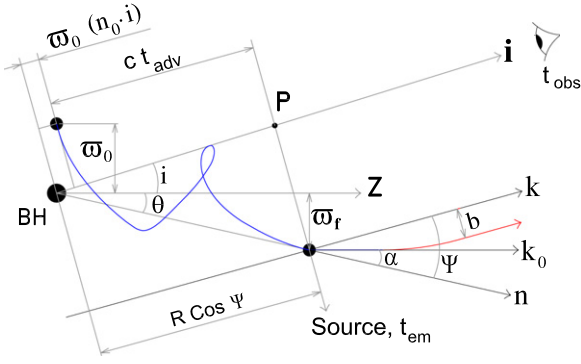
Figure 4. General helical flow geometry showing the path of the emitting source on the jet (blue) launched from the cylindrical radius ϖ_0 emitting a light ray which is subjected to the light bending effect (red). If the time of emission is $t_{\rm em}$, the time at which the signal is observed $t_{\rm obs} = (t_{\rm em} - t_{\rm adv} + \Delta t_{\rm LB})$ $(1 + z)$, where $t_{\rm adv}$ is the time taken for the source to traverse the distance $R \cos \psi$ and $\Delta t_{\rm LB}$ is the correction due to light bending effect in curved spacetime. The blob trajectory is shown in blue, emission vectors in black, and geometrical quantities including distances in grey.

inclination, and is given by

$$
\begin{aligned}
t_{\rm obs} &= \left[t_{\rm em} - t_{\rm adv} + \Delta t_{\rm LB} \right](1 + z) \\
&= \left[t_{\rm em} + (y - 1)R/c + (\boldsymbol{n_{0\cdot i}})\varpi_0/c + \Delta t_{\rm LB} \right](1 + z) \\
&= \left[t_{\rm em} - (R/c)\cos \psi + (\boldsymbol{n_{0\cdot i}})\varpi_0/c + \Delta t_{\rm LB} \right](1 + z).
\end{aligned}
\tag{48}
$$

This is used to map the time of emission to the time of observation by accounting for light bending where $\Delta t_{\rm LB}$ is the time delay from Equation (46) due to light bending and where z is the cosmological redshift of the emitting source. The effect of the time delay due to the light bending and disk inclination is to change the phase of reception of the observed signal. The phase change is expected to systematically increase as the emitting source moves along the expanding jet toward the observer. Also, we set the constant offset so that $t_{\rm obs}(t_{\rm em} = 0) = 0$ for no light bending.

4. FLOW TRAJECTORIES IN AND BEYOND ZONE 3 AND RESULTING LCs

We now discuss the construction of the LC for the variability model. The motion of the flux frozen blob is along a magnetic surface with foot points anchored on the accretion disk. A basic schematic of the blob motion along the magnetic surface is presented in Figure 5.

This surface co-rotates along with the disk at an angular frequency given by

$$
\Omega_F = \frac{c M^{1/2}}{\varpi_F^{3/2} + a M^{1/2}},
\tag{49}
$$

where a is the black hole spin parameter and ϖ_F is the cylindrical radius to the foot point from the coordinate system centered on the black hole ($z = 0$). The radius of the light cylinder ϖ_L is the position on a cylindrical surface along which the plasma moves at the speed of light and is calculated as

$$
\varpi_L = \frac{c}{\Omega_F} = \frac{\varpi_F^{3/2}}{M^{1/2}} + a.
\tag{50}
$$

The cylindrical radius from which the blob is launched is given by $\varpi_0 = f\varpi_L$, where $f = 0.1$–10. The specific angular momentum of the blob, j, is conserved along the magnetic surface. This occurs beyond the Alfvén point with a cylindrical radius $\varpi_A = x_A \varpi_L$ where $x_A^2 \leqslant 1$. The conserved angular momentum is then given by

$$
j = j_\infty = x_A^2 \varpi_L^2 \Omega_F.
\tag{51}
$$

The Ω_F in Equation (49) is the angular frequency of orbits in the Kerr metric and we make use of $a \neq 0$ only for comparison with the special relativistic model presented in Camenzind & Krockenberger (1992). For the GR models, we make use of the Schwarzschild geometry ($a = 0$) to maintain consistency with the treatment of the Doppler boost factor, aberration, and light bending.

The instantaneous position of the emitting spot is given by

$$
\mathbf{x_s} = (x, y, z) = (\varpi(t)\cos \phi(t), \varpi(t)\sin \phi(t), z(t)),
\tag{52}
$$

where ϖ is the cylindrical distance to the emitting spot from $z(t)$. In our variability model, a prescription for $\varpi = \varpi(z)$ is given by the geometry of the magnetic surface. The velocity components ($\dot{\mathbf{x}}_{\mathbf{s}} = d\mathbf{x_s}/dt$) are then

$$
\begin{aligned}
\dot{\mathbf{x}}_{\mathbf{s}} &= (\dot{x}, \dot{y}, \dot{z}) \\
&= (\dot{\varpi} \cos \phi(t) - \varpi \dot{\phi}(t), \dot{\varpi} \sin \phi(t) + \varpi \dot{\phi}(t), \dot{z}).
\end{aligned}
\tag{53}
$$

The angle between the velocity vector of the spot $\dot{\boldsymbol{x}}_s$ and the initial direction vector $\mathbf{k_0}$ is given by

$$
\begin{aligned}
\cos \xi &= \frac{\dot{\mathbf{x}}_{\mathbf{s}} \cdot \mathbf{k_0}}{|\dot{\mathbf{x}}_{\mathbf{s}}|} \\
&= \frac{1}{|\dot{\mathbf{x}}_{\mathbf{s}}|}\left(\frac{\sin \alpha}{\sin \psi}\dot{\mathbf{x}}_{\mathbf{s}} \cdot \mathbf{k} + \frac{\sin(\psi - \alpha)}{\sin \psi}\dot{\mathbf{x}}_{\mathbf{s}} \cdot \mathbf{n} \right).
\end{aligned}
\tag{54}
$$

Using the initial direction vector $\mathbf{k_0}$ from Equation (37), the final direction vector $\mathbf{k}$ from Equation (38) and the radial vector $\mathbf{n}$ from Equation (39), we can write the most general form of $\cos \xi$ as

$$
\begin{aligned}
\cos \xi &= \frac{1}{|\dot{\mathbf{x}}_{\mathbf{s}}|}\left(\frac{\sin \alpha}{\sin \psi}\dot{\mathbf{x}}_{\mathbf{s}} \cdot \mathbf{k} + \frac{\sin(\psi - \alpha)}{\sin \psi}\dot{\mathbf{x}}_s \cdot \mathbf{n} \right) \\
&= \frac{1}{|\dot{\mathbf{x}}_s|}\left\{ \frac{\sin \alpha}{\sin \psi}\left[\dot{\varpi} \cos \phi \sin i - \varpi\Omega \sin \phi \sin i + \dot{z} \cos i \right] \right. \\
&\quad + \frac{\sin(\psi - \alpha)}{\sin \psi}\dot{z}\left[\tan \theta_0 \sin \theta + \cos \theta \right] \Bigg\} \\
&= \frac{1}{|\dot{\mathbf{x}}_s|}\left\{ \dot{z}\left(\frac{\sin \alpha}{\sin \psi}\left[\tan \theta_0 \cos \phi \sin i + \cos i \right] \right.\right. \\
&\quad + \frac{\sin(\psi - \alpha)}{\sin \psi}\left[\tan \theta_0 \sin \theta + \cos \theta \right] \\
&\quad \left.\left. - \varpi\Omega \frac{\sin \alpha}{\sin \psi} \sin \phi \sin i \right) \right\}.
\end{aligned}
\tag{55}
$$

The Doppler factor D evaluated in an instantaneous stationary frame at the source using the emission vectors given
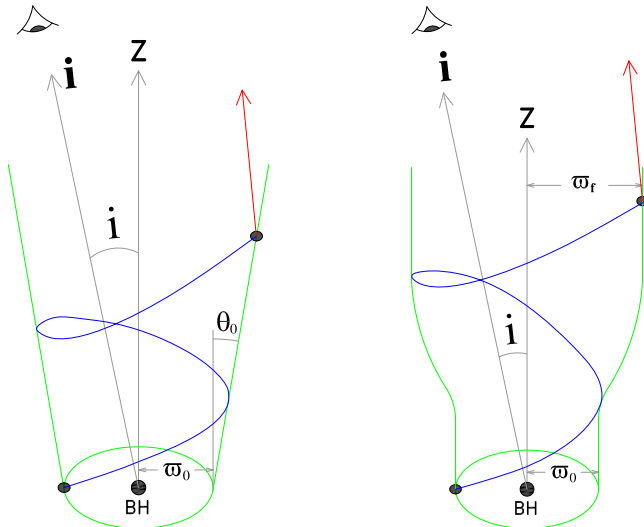
Figure 5. Helical trajectory of an emitting blob in Schwarzschild geometry, constrained along rotating magnetic field lines with footpoints on a Keplerian disk (at cylindrical radius ϖ_o). In the cone model (left plot), the half opening angle of the jet is θ_0. In the funnel model (right plot), the flow is asymptotically bound by a cylinder of radius ϖ_f at large z. The blob trajectory is shown in blue, emission vector in red, geometrical quantities including distances in grey and the jet magnetic surface shape in green.

in Equations (37), (38), and (39) is given by

$$D = \frac{1}{\gamma_{\text{jet}}\left(1 - \beta_{\text{jet}} \cos \xi\right)}. \quad (56)$$

In the observed frame, the above expression must be modified to account for the gravitational redshift. Thus, the effective redshift factor g, which is the ratio of observed to emitted energy of the emitted ray, must include the above Doppler factor as well as the gravitational redshift effect, and is given by

$$g = \frac{E_{\text{observed}}}{E_{\text{emitted}}} = (1 - 2M/R)^{1/2} D$$

$$= \frac{(1 - 2M/R)^{1/2}}{\gamma_{\text{jet}}\left(1 - \beta_{\text{jet}} \cos \xi\right)}. \quad (57)$$

An alternate derivation of the above equation is presented in the Appendix. If $\gamma_{\text{jet,i}}$ is the bulk Lorentz factor of the flow at the initial launch radius ϖ_0, the energy conservation condition along the trajectory can be written as

$$\frac{u^t}{(1 - 2M/R)} = \frac{\gamma_{\text{jet}}}{(1 - 2M/R)} = \varepsilon = \frac{\gamma_{\text{jet,i}}}{\left(1 - 2M/\varpi_0\right)} = \gamma_{\text{jet,f}}. \quad (58)$$

This can be used to express γ_{jet} in terms of the initial parameters ϖ_0 and $\gamma_{\text{jet,i}}$. From the simulations invoking radiation pressure and drag in Section 2.1, we motivate stable values of $\gamma_{\text{jet,i}} \sim 2\text{--}6$ at larger x such as the initial launching point (foot points on the disk) which we have taken to be between $(0.1\text{--}10)$ light cylinder radii. The LC is given by the spectral flux density observed $F_\nu(t)$. If F_ν' is the spectral flux density in the co-moving frame, these are related by the

expression

$$F_\nu(t) = g^\lambda(t) F_\nu'(t), \quad (59)$$

where $\lambda = 3 + \Gamma$ for a resolved blob of plasma and $\lambda = 2 + \Gamma$ for a continuous flow; Γ is the spectral index, which is the slope in the relation $F_\nu \propto \nu^\Gamma$ between the spectral flux F_ν and the emission frequency in the observer frame. Either case of λ is possible depending on the particular application to observations, but for the purposes of illustration, we take $\lambda = 2 + \Gamma$ in order to compare our results with Camenzind & Krockenberger (1992).

Because t is the time in the source frame, we obtain the time in the observer frame using the transformation in Equation (48) with the time delay Δt_{LB} to obtain $F_\nu = F_\nu(t_{\text{obs}})$ in the observer frame. The beaming effect will be prominent in the LC when the angle ξ between the initial emission vector and the velocity vector of the source is close to the disk inclination angle i between the normal drawn in the coordinate system centered on the black hole and the observer direction. The quasi-periodic behavior from orbital signatures when beaming occurs is expected to be distinctly visible in the observed LC and could last for only a few cycles.

4.1. Special Relativistic Cone Trajectory

We construct a special relativistic jet model based on that presented in Camenzind & Krockenberger (1992). The model consists of a relativistic blob in a cone geometry as shown in Figure 5. The kinematical prescription includes expressions for the cylindrical radius ϖ and the associated velocity $\dot{\varpi}$ in terms of z and $\dot{z}$. In the cone model with a jet half-opening angle θ_0,

$$\varpi = \varpi_0 + z \tan \theta_0. \quad (60)$$

Using the above equation, the velocity associated with $\varpi(t)$ is given by

$$\dot{\varpi} = \dot{z} \tan \theta_0. \quad (61)$$

The conservation of angular momentum gives an azimuthal velocity $\dot{\phi} = \Omega(t) = j_\infty/\varpi^2$ and the phase is given by $\phi(t) = \int_0^t \Omega(\tilde{t})d\tilde{t}$. The condition $\mathbf{u} \cdot \mathbf{u} = -1$ in the case of the Minkowskian metric, an approximation used in Camenzind & Krockenberger (1992) then gives

$$\left(u^t\right)^2 = \gamma_{\text{jet}}^2 = \frac{1 + u_p^2}{1 - \varpi^2 \Omega^2/c^2} = \frac{1 + u_p^2}{1 - \dfrac{j_\infty^2}{\varpi^2 c^2}}, \quad (62)$$

where $u_p = u^t(\dot{\varpi}^2 + \dot{z}^2)^{1/2}$ is the poloidal velocity. In the region where collimation of the jet occurs ($\varpi \gg \varpi_L$), the bulk Lorentz factor γ_{jet} becomes a constant due to energy conservation. Equation (33) can be written for large R because $\gamma_{\text{jet}} = \epsilon$. At large R, ϖ is also large. Hence, u_p tends to a constant value and, like Camenzind & Krockenberger (1992), we make this approximation. For a jet half-opening angle θ_0, as $\dot{z} = c u_p \cos \theta_0/\gamma_{\text{jet}}$, we obtain

$$\dot{z} = \frac{u_p}{\sqrt{1 + u_p^2}} \cos \theta_0 \left(c^2 - \frac{j_\infty^2}{\varpi^2}\right)^{1/2}. \quad (63)$$

The cylindrical distance $\varpi = \varpi(t)$ in this particular case due to the simplification of u_p being a constant. From Equation (61),

$\dot{\varpi} = \dot{z} \tan \theta_0$. Using $\dot{z}$ from Equation (63),

$$\dot{\varpi} = \frac{c u_p}{\sqrt{1 + u_p^2}} \sin \theta_0 \left(c^2 - \frac{j_\infty^2}{\varpi^2} \right)^{1/2}. \qquad (64)$$

The above expression can be written in terms of $\dot{\varpi}$ and ϖ as

$$\frac{\varpi \, \dot{\varpi}}{\sqrt{\varpi^2 - \frac{j_\infty^2}{c^2}}} = \frac{c u_p \sin \theta_0}{\sqrt{1 + u_p^2}}. \qquad (65)$$

On integrating the above equation, we obtain

$$\varpi(t) = \frac{j_\infty}{c} \left(1 + \left(\sqrt{\frac{\varpi_0^2 c^2}{j_\infty^2} - 1} + \frac{c^2 u_p}{j_\infty \sqrt{u_p^2 + 1}} \sin \theta_0 t \right)^2 \right)^{1/2}. \qquad (66)$$

The magnitude of the source velocity is given by

$$|\dot{\mathbf{x}}_\mathbf{s}| = (\mathbf{x}_\mathbf{s} \cdot \mathbf{x}_\mathbf{s})^{1/2}$$
$$= \left(\dot{\varpi}^2 + \varpi^2 \Omega^2 + \dot{z}^2 \right)^{1/2}$$
$$= \left(\dot{z}^2 \sec^2 \theta_0 + j_\infty^2 / \varpi^2 \right)^{1/2} \qquad (67)$$

In the absence of the light bending effect, $\psi = \alpha$ in which case the direction vectors $k_0 = k$. The angle between the velocity vector $\mathbf{x}_\mathbf{s}$ and the initial direction vector $\mathbf{k_0}$, $\cos \xi$ from Equation (55) then reduces to

$$\cos \xi = \frac{1}{|\dot{\mathbf{x}}_\mathbf{s}|} \Big(\dot{z} \big(\tan \theta_0 \cos \phi \sin i + \cos i \big)$$
$$- \varpi \Omega \sin \phi \sin i \Big). \qquad (68)$$

The velocity $\dot{z}$ can be obtained from Equation (63) and ϖ from Equation (66). The effective redshift factor $g(t)$ is then given by

$$g = \frac{1}{\gamma_{\text{jet}} \left(1 - \beta_{\text{jet}} \cos \xi \right)}. \qquad (69)$$

We can use $\cos \xi$ from Equation (68), γ_{jet} from Equation (62), $\beta_{\text{jet}} = \sqrt{1 - 1/\gamma_{\text{jet}}^2}$ and $\dot{\varpi}$ from Equation (66) in the above equation to obtain $g = g(t)$. The LC is given by $F(t) = g^{2+\Gamma}(t)$. Because t is the time in the source frame, we obtain the time in the observer frame using the transformation in Equation (48) without the time delay Δt_{LB} in this case to obtain $F = F(t_{\text{obs}})$ in the observer frame.

To illustrate the validity of the model developed in Section 3, we simulate an LC for a general BL Lac object using the expressions presented in this section. For this, we consider the same parameters that were considered in Camenzind & Krockenberger (1992), i.e., $u_p = 3$, $i = 0°05$, $M_\bullet = 5 \times 10^7 M_\odot$, $a = 0.8$, and $\varpi_0 = 10 \varpi_L$. The parameter $u_p = 3$ is chosen in order that $\gamma_{\text{jet,i}}$ at large $\varpi \sim 3.2$ which is within the range predicted by the effects of radiation pressure and drag in Section 2.1 and is in the same range as that considered in Camenzind & Krockenberger (1992). The resulting LC is plotted in Figure 6, which is similar to Figure 3 of Camenzind & Krockenberger (1992) with phase shift.

4.2. Fully Relativistic Cone Model

We construct a fully relativistic jet model in Schwarzschild geometry that consists of a relativistic blob in a cone geometry as shown in Figure 5. Here we consider GR effects that include time delays due to light bending, the Doppler and gravitational redshift, and the treatment of the poloidal velocity as a general function of the geometrical and kinematical parameters as opposed to the constant that was assumed in the previous case. The kinematical prescription includes expressions for the cylindrical radius ϖ and the associated velocity $\dot{\varpi}$ in terms of z and $\dot{z}$.

The cylindrical distance $\varpi(z)$ is given by Equation (60) and the velocity associated with $\varpi(z)$ is given by Equation (61). The radial distance $R(z)$ is given by

$$R(z) = \left(\varpi^2(z) + z^2 \right)^{1/2}$$
$$= \left(\varpi_0^2 + z^2 \sec^2 \theta_0 + 2 \varpi_0 z \tan \theta_0 \right)^{1/2} \qquad (70)$$

and the velocity associated with $R(z)$ is given by

$$\dot{R} = \frac{1}{R} (\varpi \, \dot{\varpi} + z \dot{z}) = \frac{\dot{z}}{R} \Big(\varpi_0 \tan \theta_0 + z \sec^2 \theta_0 \Big). \qquad (71)$$

The polar angle $\theta(z)$ is given by

$$\sin \theta(z) = \varpi(z) / R(z) \qquad (72)$$

and the velocity associated with $\theta(z)$ is given by

$$R \dot{\theta} = \frac{1}{z} \left(\dot{\varpi} - \frac{\varpi \dot{R}}{R} \right) = -\frac{\dot{z} \varpi_0}{R}. \qquad (73)$$

The conservation of angular momentum gives an azimuthal velocity $\dot{\phi} = \Omega(z) = j_\infty / \varpi^2$. Using the condition $\mathbf{u} \cdot \mathbf{u} = -1$, from Equation (35)
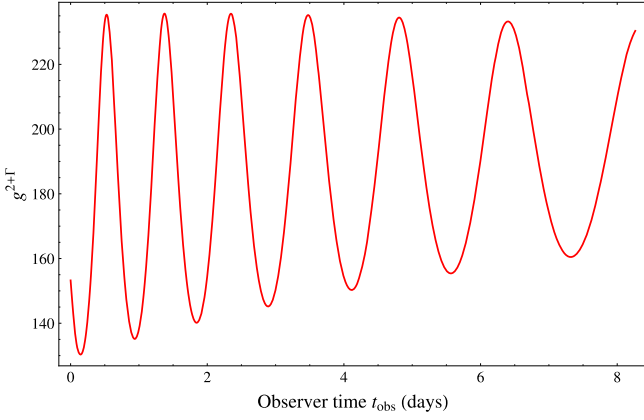
$$u^t = \gamma_{\text{jet}} = \left((1 - 2M/R) - \frac{\dot{z}^2}{R^2 c^2} \Big(\varpi_0^2 \right.$$
$$\left. + \frac{\big(\varpi_0 \tan \theta_0 + z \sec^2 \theta_0 \big)^2}{(1 - 2M/R)} \Big) - \frac{j_\infty^2}{\varpi^2 c^2} \right)^{-1/2}. \qquad (74)$$

From the energy conservation condition along the trajectory,

$$\frac{u^t}{(1 - 2M/R)} = \varepsilon = \frac{\gamma_{\text{jet,i}}}{\big(1 - 2M/\varpi_0 \big)}, \qquad (75)$$

where $\gamma_{\text{jet,i}}$ is the initial Lorentz factor. Using $\gamma_{\text{jet,i}}$ from Equation (62) for the case of $\varpi = \varpi_0$ at $z = 0$ and a constant u_p, we obtain $\gamma_{\text{jet,i}} = \left(\dfrac{1 + u_p^2}{1 - \dfrac{j_\infty^2}{\varpi_0^2 c^2}} \right)^{1/2}$ and

$$u^t = \gamma_{\text{jet}} = \gamma_{\text{jet,i}} \frac{(1 - 2M/R)}{\big(1 - 2M/\varpi_0 \big)}. \qquad (76)$$

Figure 6. Simulated light curve for $u_p = 3$, $x_A = 0.9$, $i = 0°\!.05$, $M_\bullet = 5 \times 10^7 \, M_\odot$, $a = 0.8$, $\varpi_0 = 10\varpi_L$, and $\Gamma = 1$. The light curve (red curve) shows the quasi-periodic oscillation expected from a general BL Lac object when the special relativistic formalism is used in the simulation.

Using the above expression for u^t in Equation (74), we obtain an equation for $\dot{z}$ given by

$$
\dot{z} = cR\left((1 - 2M/R) - \frac{j_\infty^2}{\varpi^2 c^2} - \frac{(1 - 2M/\varpi_0)^2}{(1 - 2M/R)^2} \frac{1}{\gamma_{\mathrm{jet,i}}^2} \right)^{1/2}
$$
$$
\times \left(\varpi_0^2 + \frac{\left(\varpi_0 \tan\theta_0 + z \sec^2\theta_0 \right)^2}{(1 - 2M/R)} \right)^{-1/2}.
$$
$$(77)$$

In the above equation, $\varpi = \varpi(z)$ from Equation (60) and $R = R(z)$ from Equation (70). The above expression can be integrated to obtain $z = z(t)$ as

$$
\int_0^z \frac{dz}{R}
$$
$$
\times \left(\frac{\varpi_0^2 + \dfrac{\left(\varpi_0 \tan\theta_0 + z \sec^2\theta_0 \right)^2}{(1 - 2M/R)}}{(1 - 2M/R) - \dfrac{j_\infty^2}{\varpi^2 c^2} - \dfrac{(1 - 2M/\varpi_0)^2}{(1 - 2M/R)^2} \dfrac{1}{\gamma_{\mathrm{jet,i}}^2}} \right)^{1/2}
$$
$$
= c \int_0^t dt.
$$
$$(78)$$

Once we obtain $z = z(t)$, this can be used to evaluate $\dot{z} = \dot{z}(z(t))$, $\varpi = \varpi(z(t))$, and $\dot{\varpi} = \dot{\varpi}(z(t))$. The magnitude of the source velocity is given by

$$
|\dot{\mathbf{x}}_s| = (\dot{\mathbf{x}}_s \cdot \dot{\mathbf{x}}_s)^{1/2} = \left(\dot{\varpi}^2 + \varpi^2 \Omega^2 + \dot{z}^2 \right)^{1/2}
$$
$$
= \left(\dot{z}^2 \sec^2\theta_0 + j_\infty^2 / \varpi^2 \right)^{1/2}.
$$
$$(79)$$

The velocity $\dot{z} = \dot{z}(z(t))$ and all other terms in the above expression can be cast in terms of $z(t)$. In the current model, we consider the light bending effect in which case the direction vector $\mathbf{k_0}$ is obtained from Equation (37) and the angle between the velocity vector $\mathbf{x}_s$ and the initial direction vector $\mathbf{k_0}$, given by $\cos\xi$, is given by the general expression in Equation (55).

The effective redshift factor $g(t)$ is then given by the general expression in Equation (57). We can use $\cos\xi$ from Equation (55), γ_{jet} from Equation (74), and β_{jet} from Equation (36) in the equation for g to obtain $g = g(t)$. The LC is given by $F(t_{\mathrm{obs}}) = g^{2+\Gamma}(t_{\mathrm{obs}})$, expressing t in terms of t_{obs}. The importance of making use of a fully relativistic model when compared to the earlier special relativistic model is presented in terms of the difference between the t_{obs} in both cases. It is seen that for the fully relativistic model, t_{obs} tends to increase systematically with t_{em}. This difference in timescale is of the order of $\sim$5 days by the end of the simulation. This difference is plotted in Figure 7, which justifies the use of the fully relativistic model.

To illustrate the model developed in Section 3 and the comparison with the special relativistic cone case in Section 4.1, we simulate an LC for a general BL Lac object using the expressions presented in this section. Using again $u_p = 3$ as an initial condition, with $i = 0°\!.05$, $M_\bullet = 5 \times 10^7 \, M_\odot$, $a = 0.8$, and $\varpi_0 = 10\varpi_L$, the resulting LC is shown in Figure 8. The parameter $u_p = 3$ is chosen in order that $\gamma_{\mathrm{jet,i}}$ at large $\varpi \sim 3.2$, which is within the range predicted by the effects of radiation pressure and drag in Section 2.1 and is in the same range as that considered in Camenzind & Krock-enberger (1992). This is a comparison between the LCs in the fully relativistic cone case and the special relativistic case, which indicates an increased amplitude in the former. There is also a systematically increasing phase lag compared to the latter case as expected due to the effect of the time delay caused by light bending. The ratio of the amplitudes gives a 12% increase in the maximum amplitude due to the GR boost factor in g. The beaming effect is observed for the last two cycles for the GR cone case where there is an increased amplitude, which then settles down. The increased amplitude ratio and the phase lag change can be attributed to the integrals over time of intensity and phase amplifying the small but early differences in phase. Even a small phase difference between the GR and special relativistic simulations gets amplified due to the nature of the g factor in Equation (57), which includes the gravitational redshift factor $(1 - 2M/R)^{1/2}$ and light bending effects.

4.3. Fully Relativistic Funnel Model

We construct a GR (Schwarzschild geometry) jet model which consists of a relativistic blob in a funnel geometry as shown in Figure 5. The shape of the magnetic surface can be determined by solving the relativistic Grad–Shafranov equation (e.g., Fendt & Memola 2001). This is expected to yield stable, axisymmetric magnetic field configurations. Here, we make an approximation of this shape and impose the condition of angular momentum conservation along this surface. Here too, we consider the GR effects, which include the time delay due to light bending, the Doppler and gravitational redshift, and the treatment of the poloidal velocity as a general function of the geometrical and kinematical parameters as opposed to a constant that is assumed in the special relativistic case. The kinematical prescription includes expressions for the cylindrical radius ϖ and the associated velocity $\dot{\varpi}$ in terms of z and $\dot{z}$. The cylindrical distance $\varpi(z)$ is given by

$$
\varpi(z) = \varpi_0 \left(1 + k \left(1 - e^{-z/z_f} \right) \right),
$$
$$(80)$$
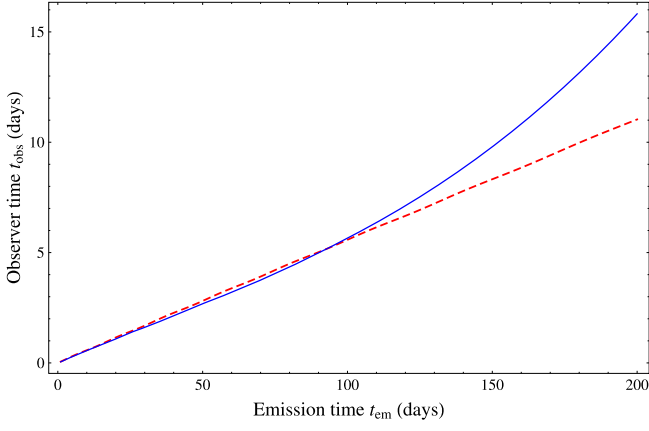
Figure 7. Curves showing t_{obs} vs. t_{em} for the fully relativistic cone model (blue) and the special relativistic cone model (red dashed). The t_{obs} in the former increases systematically and reaches a difference of $\sim$5 days by the end of the simulation with respect to the latter.

Figure 8. Simulated light curve for $u_p = 3$, $x_A = 0.9$, $i = 0°.05$, $M_\bullet = 5 \times 10^7 M_\odot$, $a = 0.8$, $\varpi_0 = 10\varpi_L$, and $\Gamma = 1$. The light curve shows the quasi-periodic oscillation expected from a general BL Lac object. A general relativistic light curve from orbital features in a cone geometry (blue curve) is compared with the previously calculated special relativistic light curve from orbital features in a cone geometry (red curve).The increased amplitude ratio and the phase lag change can be attributed to the integrals over time of intensity and phase amplifying the small but early differences in phase. Even a small phase difference between the general relativistic and special relativistic simulations gets amplified due to the nature of the g factor in Equation (57) which includes the gravitational redshift factor $(1 - 2M/R)^{1/2}$ and light bending effects.

where $k = (\varpi_f - \varpi_0)/\varpi_0$, ϖ_f is the cylindrical distance between the normal axis and the source position at the location where the funnel transitions into a cylinder. If we use $\varpi_f = q\varpi_L$,

$$k_f = (\varpi_f - \varpi_0)/\varpi_0 = q/f - 1. \tag{81}$$

A constraint on z_f can also be obtained based on the vertical distance z at the region where $\varpi = \varpi_f$. If the jet half opening angle is θ_0, $\tan\theta_0 = (\varpi_f - \varpi_0)/z_f$, then

$$z_f = (q - f)\varpi_L/\tan\theta_0. \tag{82}$$

The velocity associated with ϖ (z) is given by

$$\dot{\varpi} = \dot{z}\frac{\varpi_0 k}{z_f}e^{-z/z_f} \tag{83}$$

The radial distance $R(z)$ is given by

$$R(z) = \left(\varpi^2(z) + z^2\right)^{1/2}$$
$$= \left(\varpi_0^2\left(1 + k\left(1 - e^{-z/z_f}\right)^2 + z^2\right)^{1/2} \tag{84}$$
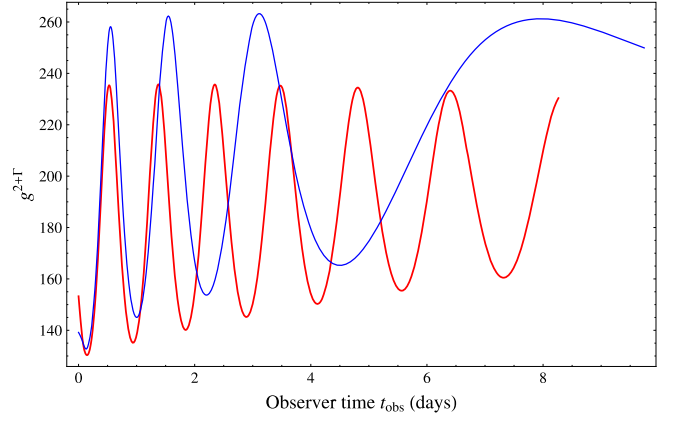
and the velocity associated with $R(z)$ is given by

$$\dot{R} = \frac{1}{R}(\varpi\,\dot{\varpi} + z\dot{z})$$
$$= \frac{\dot{z}}{R}\left(\frac{\varpi_0^2 k}{z_f}\left(1 + k\left(1 - e^{-z/z_f}\right)e^{-z/z_f} + z\right). \tag{85}$$

As before, the polar angle $\theta(z)$ is given by

$$\sin\theta(z) = \varpi(z)/R(z) \tag{86}$$

and the velocity associated with $\theta(z)$ is given by

$$R\dot{\theta} = \frac{1}{z}\left(\dot{\varpi} - \frac{\varpi\,\dot{R}}{R}\right)$$
$$= \frac{\dot{z}\varpi_0}{R}\left(ke^{-z/z_f}\left(z/z_f + 1\right) - (1 + k)\right). \tag{87}$$

The conservation of angular momentum gives an azimuthal velocity $\dot{\phi} = \Omega(z) = j_\infty/\varpi^2$. The condition $\mathbf{u}\cdot\mathbf{u} = -1$ in case of the Schwarzschild metric gives

$$u^t = \left[(1 - 2M/R) - \frac{j_\infty^2}{\varpi^2 c^2}\right.$$
$$- \frac{\dot{z}^2}{R^2 c^2}\left\{\left(\frac{\varpi_0^2 k}{z_f}\left(1 + k\left(1 - e^{-z/z_f}\right)\right)e^{-z/z_f} + z\right)^2\right.$$
$$\left.\left. + \varpi_0^2\left(ke^{-z/z_f}\left(z/z_f + 1\right) - (1 + k)\right)^2\right\}\right]^{-1/2}. \tag{88}$$

Using the general expression for u^t from Equation (74), we obtain an equation for $\dot{z}$ given by

$$\dot{z} = cR\left((1 - 2M/R) - \frac{j_\infty^2}{\varpi^2 c^2} - \frac{(1 - 2M/\varpi_0)^2}{(1 - 2M/R)^2}\frac{1}{\gamma_{\text{jet,i}}^2}\right)^{1/2}$$
$$\left[\left(\frac{\varpi_0^2 k}{z_f}\left(1 + k\left(1 - e^{-z/z_f}\right)\right)e^{-z/z_f} + z\right)^2\right.$$
$$\left. + \varpi_0^2\left(ke^{-z/z_f}\left(z/z_f + 1\right) - (1 + k)\right)^2\right]^{-1/2}. \tag{89}$$

In the above equation, $\varpi = \varpi(z)$ from Equation (80) and $R = R(z)$ from Equation (84). The above expression can be

integrated to obtain $z = z(t)$ as

$$\int_0^z \frac{dz}{R} \left\{ \frac{\left[\left(\frac{\varpi_0^2 k}{z_f}\left(1 + k\left(1 - e^{-z/z_f}\right)\right)e^{-z/z_f} + z\right)^2\right.}{\left. + \varpi_0^2\left(ke^{-z/z_f}\left(z/z_f + 1\right) - (1+k)\right)^2\right]^{1/2}}{\left(1 - 2M/R\right) - \frac{j_\infty^2}{\varpi^2 c^2} - \frac{(1-2M/\varpi_0)^2}{(1-2M/R)^2}\frac{1}{\gamma_{\rm jet,i}^2}} \right\} = c\int_0^t dt.$$

(90)

If we use k from Equation (81) and z_f from Equation (82), we can obtain $z = z(t)$, which can then be used to evaluate $\dot{z} = \dot{z}(z(t))$, $\varpi = \varpi(z(t))$, and $\dot{\varpi} = \dot{\varpi}(z(t))$. The magnitude of the source velocity is given by

$$|\dot{\mathbf{x}}_s| = (\mathbf{x}_s \cdot \mathbf{x}_s)^{1/2} = \left(\dot{\varpi}^2 + \varpi^2\Omega^2 + \dot{z}^2\right)^{1/2}$$

$$= \left(\dot{z}^2\left(\frac{\varpi_0^2 k^2}{z^2}e^{-2z/z_f} + 1\right) + j_\infty^2/\varpi^2\right)^{1/2}.$$

(91)

Once we obtain $z = z(t)$, this can be used to evaluate $\dot{z} = \dot{z}(z(t))$, $\varpi = \varpi(z(t))$, and $\dot{\varpi} = \dot{\varpi}(z(t))$. The velocity $\dot{z} = \dot{z}(z(t))$ and all other terms in the above expression can be cast in terms of $z(t)$. In the current model, we consider the light bending effect in which case the direction vector $\mathbf{k_0}$ is obtained from Equation (37) and the angle between the velocity vector $\mathbf{x}_s$ and the initial direction vector $\mathbf{k_0}$ given by $\cos\xi$ is given by the general expression in Equation (55).

The effective redshift factor $g(t)$ is then given by the general expression in Equation (57). We can use $\cos\xi$ from Equation (55), $\gamma_{\rm jet}$ from Equation (74), and $\beta_{\rm jet}$ from Equation (36) in the equation for g to obtain $g = g(t)$. The LC is given by $F(t_{\rm obs}) = g^{2+\Gamma}(t_{\rm obs})$, expressing t in terms of $t_{\rm obs}$. In this case as well, $t_{\rm obs}$ tends to increase systematically with $t_{\rm em}$, analogous to the full relativistic cone case. Though, the change is slightly gradual. This difference in timescale is of the order of ~ 3 days by the end of the simulation. This difference is plotted in Figure 9; clearly the use of the fully relativistic model impacts the phase significantly.

To illustrate the model developed in Section 3 and the comparison with the special relativistic cone case in Section 4.1, we simulate an LC for a general BL Lac object using the expressions presented in this section. Using once again $u_p = 3$ as an initial condition, $i = 0°05$, $M_\bullet = 5 \times 10^7 M_\odot$, $a = 0.8$, and $\varpi_0 = 10\varpi_L$, the LC is plotted in Figure 10. The parameter $u_p = 3$ is chosen in order that $\gamma_{\rm jet,i}$ at large $\varpi \sim 3.2$, which is within the range predicted by the effects of radiation pressure and drag in Section 2.1 and is in the same range as that considered in Camenzind & Krockenberger (1992). A comparison between the LCs in the GR cone case and the special relativistic case indicates an increased amplitude in the former in the funnel geometry as well; there is also a systematically increasing phase lag compared to the latter case as expected due to the effect of the time delay caused by light bending. The ratio of the amplitudes gives a 12% increase in the maximum amplitude due to the GR boost factor in g justifying the use of a fully relativistic model. Thus, the beaming effect is observed for the first two cycles for the GR funnel case where there is an increased amplitude, which then settles down. The increased amplitude ratio, and the phase lag change here as well, can be attributed to the integrals over time of intensity and phase amplifying the small but early

differences in phase. Even a small phase difference between the GR and special relativistic simulations gets amplified due to the nature of the g factor in Equation (57), which includes the gravitational redshift factor $(1 - 2M/R)^{1/2}$ and light bending effects.

A comparison is then done between the simulated LC in funnel and cone geometries for the GR formalism. For the parameter values $\gamma_{\rm jet,i} = 4$, $k = 2$ $(q/f = 3)$, $\theta_0 = 0°1$, $i = 5°$, $M_\bullet = 5 \times 10^7 M_\odot$, $a = 0$, and $\varpi_0 = 10\varpi_L$, the LCs are plotted in Figure 11. The phase of the funnel geometry curve systematically lags the phase of the cone geometry curve indicating a dominance by higher frequencies. This phase shift is seen to increase with the simulation time. The ratio of the maximum amplitude of the funnel geometry curve to that of the maximum amplitude of the cone geometry curve is 9%. Because of the slower expansion of the funnel compared to the cone, there are more orbits at higher frequencies (due to conservation of angular momentum) at a location where the GR boost factor is more effective.

4.4. Funnel Model Simulations and Discussion

We perform two sets of simulations to address the expected LC and timing information for an observer viewing the AGN at varying inclination angles i, black hole mass $M_\bullet$, and the initial launch bulk Lorentz factor $\gamma_{\rm jet,i}$. The choices for i are based on typical values expected for the inclination angle from observational studies (e.g., Pushkarev et al. 2009). A time series analysis of the LC is conducted using the Fourier periodogram analysis (e.g., Mohan et al. 2014; Mohan & Mangalam 2014) and the wavelet analysis (e.g., Torrence & Compo 1998; Mohan et al. 2011). The Fourier periodogram of the LC is the normalized Fourier power spectrum, evaluated at the frequencies $f = j/(N\Delta t)$ where $j = 1, 2, ...(N/2 - 1)$ (up to and excluding the Nyquist frequency) and is fit with a power-law shape, $P(f) = Af^m$, assumed to be the shape that best describes the underlying PSD. The wavelet analysis gives the QPO and its evolution including the phases during which it is present in the LC, and hence the number of cycles it is present for. In the wavelet analysis, any periodicity inside a cone of influence (triangular region) can be trusted. Features outside this region could be subject to systematic effects due to the wavelet method. From these simulations, we aim to address questions such as the typical QPO expected from orbital processes in the jet, its dependence on $M_\bullet$, the beaming effect, the conditions for its sustenance and the typical range of PSD slopes expected. These are motivated from observational studies at optical and radio wavelengths which indicate QPOs with timescales of less than a day to a few tens of days (e.g., Gupta et al. 2012).

We first simulate the expected LC from an emitting source in helical motion along the funnel shaped magnetic surface launched from a single ring with cylindrical radius $\varpi = 10\varpi_L$. The other quantities that are fixed include $k = 2$, $x_A = 0.9$, $\theta_0 = 0°1$ and $\alpha = 1$. The simulations are carried out for $i = 3°$, $6°$, $9°$, $12°$ and, $15°$ with $M_\bullet = (0.5, 5) \times 10^8 M_\odot$ and $\gamma_{\rm jet,i} = 2$ (mildly relativistic), 4 (relativistic), and 10 (highly relativistic). The choice of $\gamma_{\rm jet,i} = 2$, 4 is consistent with the range predicted by the effects of radiation pressure and drag in Section 2.1. The choice of $\gamma_i = 10$ was made in order to study simulated LCs for jets from black holes with higher masses, which include
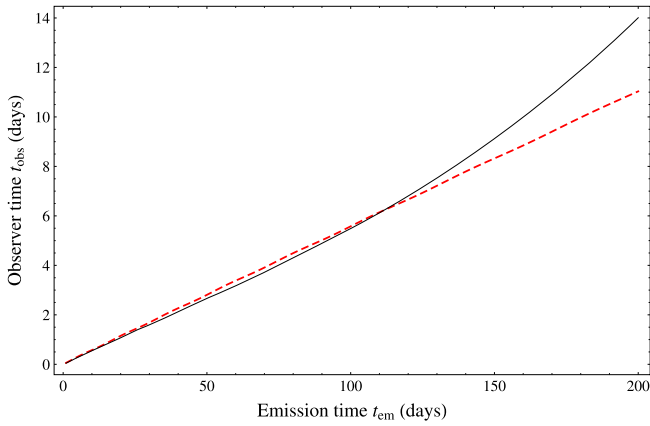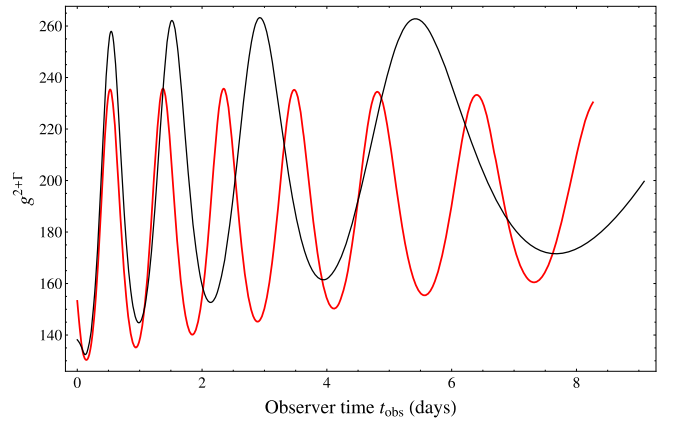
Figure 9. Curves showing t_{obs} vs. t_{em} for the fully relativistic funnel model (black) and the special relativistic cone model (red dashed). The t_{obs} in the former increases systematically and reaches a difference of ~3 days by the end of the simulation with respect to the latter.

Figure 10. Simulated light curve for $u_p = 3$, $x_A = 0.9$, $i = 0°05$, $M_\bullet = 5 \times 10^7 M_\odot$, $a = 0.8$, $\varpi_0 = 10\varpi_L$, and $\Gamma = 1$. The light curve shows the quasi-periodic oscillation expected from a general BL Lac object. A general relativistic light curve from orbital features in a funnel geometry (black curve) is compared with the previously calculated special relativistic light curve from orbital features in a cone geometry (red curve). The increased amplitude ratio and the phase lag change can be attributed to the integrals over time of intensity and phase amplifying the small but early differences in phase. Even a small phase difference between the general relativistic and special relativistic simulations gets amplified due to the nature of the g factor in Equation (57), which includes the gravitational redshift factor $(1 - 2M/R)^{1/2}$ and light bending effects.

blazars. The results of the timing analysis are summarized in Table 1 and some interesting cases are plotted in Figure 12.
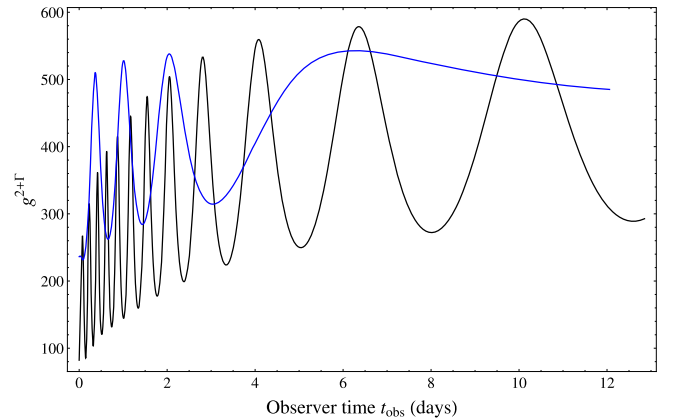
With an increase in the inclination angle i, the maximum amplitude in the simulated LC tends to decrease. This is due to the beaming effect because the projection of the emitting source velocity onto the emission direction ($\beta_{jet} \cdot \mathbf{k}$) continues to grow smaller in the direction toward the observer. This leads to a less pronounced maximum amplitude that continues to decrease with an increase in i. For a given $M_\bullet$, the maximum amplitude tends to increase with $\gamma_{jet,i}$. This is due to the stronger beaming effect toward the observer's line of sight by the emitting source for larger $\gamma_{jet,i}$. The PSD slope ranges between −1.54 and −3.43. The slopes steeper than −2.5 are likely to be the result of a poor fit. Hence, we calculate a median slope of -2.00 ± 0.28. QPOs peaked between 20.7–130.7 days are inferred from the wavelet and PSD analysis. For a given $M_\bullet$, the QPO peak shifts to higher values with increasing i. This is due to the orientation away from the observer's line of sight for the chosen set of parameters leading to the larger timescale QPO at larger r.

We then simulate the expected LC from multiple emitting sources in helical motion along the funnel shaped magnetic surface launched from rings with cylindrical radii $\varpi = 5, 6, 7,$ and $8\ \varpi_L$. Fixed parameters in this simulation include $k = 2$, $x_A = 0.9$, $\theta_0 = 0°1$, and $\alpha = 1$. The simulations are carried out for $i = 3°, 6°, 9°, 12°,$ and $15°$ with $M_\bullet = (0.5, 5) \times 10^8 M_\odot$ and $\gamma_{jet,i} = 2$–10 as in the previous case. The results of the timing analysis are summarized in Table 2 and some interesting cases are plotted in Figure 13.

In these simulations, we observe similar trends as those that were present in the previous case. With an increase in i, the maximum amplitude in the simulated LC tends to decrease. For a given $M_\bullet$, the maximum amplitude tends to increase with $\gamma_{jet,i}$. The PSD slope in these simulations is more well constrained and ranges between −1.09 and −3.39. The slopes steeper than −2.5 are likely to be the result of a poor fit. Hence, we calculate a median slope of -2.02 ± 0.34. Significant QPOs ranging between 1.37–33.49 days are detected in these simulations. The QPO for high $\gamma_{jet,i}$ tends to be lower than that for lower $\gamma_{jet,i}$. This is likely because, for

Figure 11. Simulated light curve for $\gamma_{jet,i} = 4$, $k = 2$, $x_A = 0.9$, $i = 0°05$, $M_\bullet = 5 \times 10^7 M_\odot$, $a = 0$, and $\varpi_0 = 10\varpi_L$. A comparison is made between the funnel geometry light curve (black curve) and the cone geometry light curve (blue curve). Both light curves show a quasi-periodic oscillation expected from a general BL Lac object. The phase of the funnel geometry curve systematically lags the phase of the cone geometry curve. Also, the funnel geometry curve is dominated by higher frequencies in the initial portion.

high γ_{jet}, the beamed portion occurs in the inner jet close to the black hole where the orbital frequency is higher due to gravitational redshift. Thus, the associated timescales are then expected to be lower. Thus, the power spectrum is dominated by higher frequencies, which implies that the PSD would tend to flatten. This trend is also seen in the above multiple emitting ring simulations for $M_\bullet = 5 \times 10^7 M_\odot$. For the case of $M_\bullet = 5 \times 10^8 M_\odot$, the opposite trend is seen. For a higher $M_\bullet$, there are more cycles during beaming due to

favorable orientation (at higher frequencies); hence, the PSD slope tends to steepen.

5. SUMMARY AND CONCLUSIONS

We summarize our results. The special relativistic cone model (Section 4.1) is the same as that proposed by Camenzind & Krockenberger (1992). The fully relativistic models developed in this work include the cone model (Section 4.2) and the funnel model (Section 4.3). The main results include discussions on the novel aspects of the fully relativistic funnel model with respect to the special relativistic cone model.

1. We have considered a possible mechanism of jet-based variability from various sources including BL Lac objects and blazars (e.g., Camenzind & Krockenberger 1992; Steffen et al. 1995), quasars (e.g., Kudryavtseva et al. 2011), binary black holes (e.g., Iguchi et al. 2010), and X-ray binaries (e.g., Fukumura & Kazanas 2008; Fukumura et al. 2009). We extended the light-house model proposed in Camenzind & Krockenberger (1992), which was applied to simulate optical LCs from BL Lac objects and quasars.

2. We studied the effects of radiation pressure and drag and derived the saturation Lorentz factors that are achievable. The Lorentz factors γ range 2–7 in the purely radial outflow simulations. For a poloidal flow $(\beta_\phi = 0)$, we obtain γ in the range 1.1–26.3, greater than that previously obtained. Though, the drag force acting on the non-radial component of the blob velocity plays an important role in rapidly decreasing $\gamma \sim 2$, thus stabilizing it at very small x, indicating that the outflow is stable even in the innermost regions. Thus, the $\gamma_{\rm jet,i}$ chosen for the simulations in the relativistic cone and funnel models in the subsequent section can be obtained at larger distances with small to moderately relativistic emitting blob velocities.

3. We constructed a kinematic model of orbital blobs along helical trajectories on a magnetic surface approximating the expanding jet with foot points on the accretion disk in the vicinity of a black hole using a special relativistic calculation of the g factor for cone geometry similar to Camenzind & Krockenberger (1992) in Section 4.1 and a fully relativistic formulation in cone geometry (Section 4.2) and the same in a more realistic funnel geometry (Section 4.3). The g factor was calculated in Schwarzschild geometry and the following GR effects were included: gravitational and Doppler shifts, aberration, and a prescription for time delay due to orientation and light bending.

4. By using the periodogram and wavelet based time series analysis techniques (Section 4.4), we seek to distinguish among the various flavors of the generic jet variability model, which here include the cone and funnel models. The time series analysis of simulated LCs yields properties including aperiodic variability, its timescales, and the emission region; the PSD slope and its range, which can be compared with observations in optical/UV and X-ray. It is also found that the QPO, its evolution, and stability can be described by the orbital motion of blobs in the jet.

Table 1
Results for Light Curves from Blobs Launched from
a Single Ring of Cylindrical Radius $\varpi_0 = 10\varpi_L$

Inclination Angle i (°)	$\dfrac{M_\bullet}{10^8\,M_\odot}$	$\gamma_{\rm jet,i}$	Max. Amplitude A	PSD Slope m	QPO (days)
3	0.5	2	54.48	−1.96	124.0 W
...	...	4	506.49	−1.97	89.8 W
...	...	10	8090.84	−2.26	79.7 W
...	5	2	54.24	−1.54	68.2
...	...	4	492.43	−1.65	18.6
...	...	10	6949.31	−1.82	...
6	0.5	2	54.05	−2.42	124.8 W
...	...	4	483.05	−2.18	90.8 W
...	...	10	5780.68	−3.00	80.8 W
...	5	2	54.06	−1.64	70.1
...	...	4	483.10	−1.73	20.7
...	...	10	5780.68	−2.01	...
9	0.5	2	51.50	−1.70	126.2 W
...	...	4	372.24	−2.30	92.4 W
...	...	10	1540.67	−3.16	82.5 W
...	5	2	51.51	−1.70	73.2
...	...	4	372.25	−1.77	24.3
...	...	10	1544.25	−2.03	...
12	0.5	2	46.60	−1.73	128.2 W
...	...	4	238.24	−2.42	94.8
...	...	10	328.10	−3.13	85.0 W
...	5	2	46.60	−1.73	77.5
...	...	4	238.24	−1.80	29.0
...	...	10	328.56	−1.98	...
15	0.5	2	40.24	−3.43	130.7 W
...	...	4	136.38	−2.50	97 W
...	...	10	81.36	−3.07	88.1 W
...	5	2	40.25	−1.75	82.9
...	...	4	136.38	−1.82	35.1
...	...	10	81.44	−1.94	

Note. The parameters used that are not reported in the above table include x_A=0.9, $\theta_0 = 0°1$ and $\alpha = 1$. The slopes steeper than −2.5 are likely to be the result of a poor fit. Hence, we calculate a median slope of -2.00 ± 0.28 and the QPO estimates range between 20.7 and 130.7 days. A W next to a QPO peak indicates its measurement using the wavelet analysis only. If there is nothing present next to the inferred QPO, the measurement is the mean of the wavelet and PSD estimates.

5. The use of fully relativistic models (given in Section 4.2 and Section 4.3) was justified by the resulting amplitude increase (by about 12 %) due to the GR boosts and a systematically increasing phase lag in the simulated LC for a general BL Lac object from the fully relativistic funnel when compared to the special relativistic cone, which occurs at small k and larger inclination angles i. The phase lag has been explained by the angular momentum conservation in combination with the gradual increase of the orbital radius. Our fully relativistic formulation reduces to the special relativistic formulation in the limit of large R and when all the above GR effects are not considered; this is presented in Section 4.

6. There is thus a necessity to account for all GR effects as used in the present model for the correct description of the physical effects on emitted radiation from these jetted sources and to use more realistic jet geometries. It can be thus applied to both timing studies of jet variability as well as to map trajectories of radio blobs or blobs in the
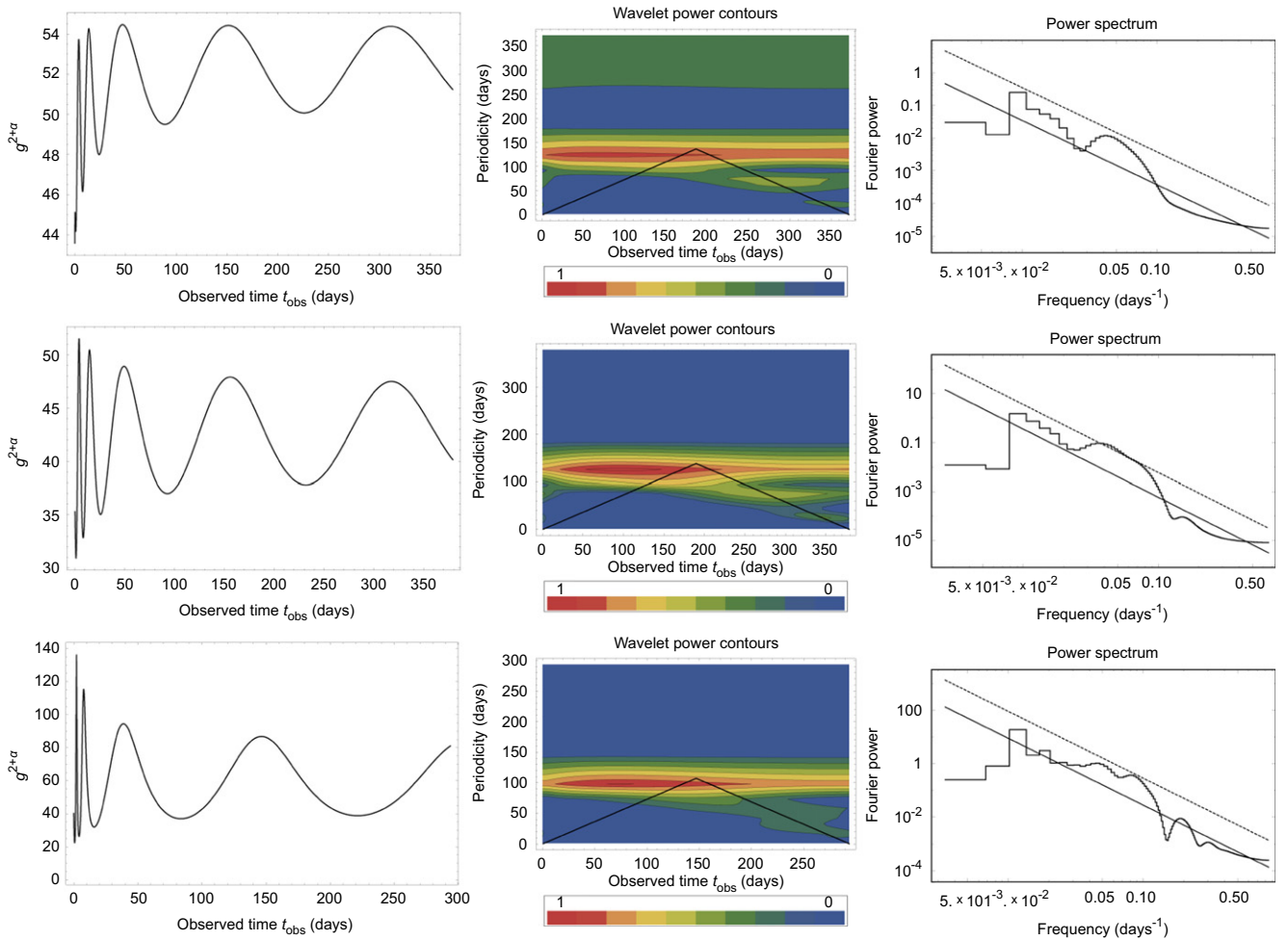
Figure 12. Results for light curves from a single emitting ring of $\varpi_0 = 10\varpi_L$. The plots in the left column are the simulated light curves, the plots in the middle column are their wavelet analyses, and the plots in the right column are their PSD. The PSD is fit with a power law with a slope m. The line above the best fit indicates a 99% significance on any inferred QPO period. Top row: simulation for $i = 3°$, $M_\bullet = 5 \times 10^7 M_\odot$, $\gamma_{jet} = 2$; a QPO of 124 days is inferred from the timing analyses; a PSD slope of -1.96 is inferred. Middle row: simulation for $i = 9°$, $M_\bullet = 5 \times 10^7 M_\odot$, $\gamma_{jet} = 2$; a QPO of 126.2 days is inferred from the timing analyses; a PSD slope of -2.78 is inferred. Bottom row: simulation for $i = 15°$, $M_\bullet = 5 \times 10^7 M_\odot$, $\gamma_{jet} = 4$; a QPO of 97 days is inferred from the timing analyses; a PSD slope of -2.50 is inferred.

inner jet and compared with observations to help identify the region of emission. The application of the model to radio data is being planned.

7. Two sets of simulations, one for blobs emanating from a single and another from multiple rings were carried out to span a range of LCs. Their timing properties were studied for the maximum amplitudes, PSD slope, and QPO if present. Two main trends are observed in the single emitting ring simulations. With an increase in the inclination angle i, the maximum amplitude in the simulated LC tends to decrease, because the beaming effect in the direction of the observer continues to grow smaller. The other trend is that for a given $M_\bullet$, the maximum amplitude tends to increase with $\gamma_{jet,i}$, due to the stronger beaming effect toward the observer's line of sight by the emitting source for larger $\gamma_{jet,i}$. We calculate a median slope of -2.00 ± 0.28 similar to the observed PSD slopes of blazars in the Optical and X-ray translated to the source frame. QPOs peaked between 20.7–130.7 days are inferred from the wavelet and PSD

analysis. The second set of simulations were carried out for a blob launched from multiple emitting rings $\varpi_0 = 5 - 8\varpi_L$. In these multiple emitting rings simulations, the same two trends above are observed. We calculate a median slope of -2.02 ± 0.34. Significant QPOs ranging between 1.37–33.49 days are detected in these simulations. In the multiple emitting rings simulations, we were also able to identify QPOs because a wider choice of orientations result from a larger set of initial conditions; the same trends were observed in the relationship between the QPO timescale, $M_\bullet$, and γ_{jet}. The QPO timescale tends to reduce with an increase in γ_{jet} due to a GR boost, which tends to flatten the PSD slope. Aperiodic variability when considering multiple emitting rings is a natural consequence that is seen in our results.

A natural power-law-shaped PSD with a typical slope of approximately -2 along with a weak to strong QPO, ranging between 1.37 and 130.7 days, emerges from the simulations

Table 2
Results for Light Curves from Blobs Launched from
Multiple Rings of Cylindrical Radii $\varpi_0 = 5 - 8\varpi_L$

Inclination Angle i (°)	$\dfrac{M_\bullet}{10^8 M_\odot}$	$\gamma_{jet,i}$	Max. Amplitude A	PSD Slope m	QPO (days)
3	0.5	2	54.35	−2.01	…
…	…	4	494.97	−1.67	…
…	…	10	5955.14	−1.70	…
…	5	2	47.94	−1.72	27.62
…	…	4	327.01	−1.90	7.89
…	…	10	1909.06	−1.77	1.37
6	0.5	2	52.28	−2.47	…
…	…	4	424.37	−1.73	…
…	…	10	4155.13	−1.96	0.98
…	5	2	47.43	−1.95	28.34
…	…	4	338.99	−2.02	4.37, 8.74
…	…	10	3553.40	−2.36	1.81
9	0.5	2	48.46	−2.81	…
…	…	4	322.86	−1.81	…
…	…	10	2778.43	−1.31	…
…	5	2	45.01	−2.12	14.80, 29.59
…	…	4	298.02	−2.18	5.06, 10.13
…	…	10	2778.43	−3.18	…
12	0.5	2	44.00	−2.99	…
…	…	4	217.66	−2.00	…
…	…	10	962.85	−1.09	…
…	5	2	40.96	−2.39	15.65, 31.31
…	…	4	218.57	−2.34	6.03
…	…	10	962.85	−3.39	…
15	0.5	2	38.23	−2.94	5.45
…	…	4	135.59	−1.97	…
…	…	10	207.60	−1.23	…
…	5	2	35.78	−2.61	16.74, 33.49
…	…	4	137.58	−2.46	2.89, 7.22
…	…	10	207.60	−3.24	1.89

Note. The parameters used that are not reported in the above table include $x_A = 0.9$, $\theta_0 = 0°1$ and $\alpha = 1$. We calculate a median slope of $−2.02 \pm 0.34$ and the QPO estimates range between 1.37 and 33.49 days. All QPOs inferred above are the mean of the wavelet and PSD estimates.

considering single and multiple emitting rings. This shape comes naturally considering only geometrical parameters, even before any consideration of physical models of the orbital instabilities. The detailed magnetic structure can be constructed by solving the relativistic Grad–Shafranov equation. The dynamical timescale due to jet-based orbital processes is expected to be from a few minutes to tens of days depending on the black hole mass. The GR funnel model for variability can thus be applied to radio, optical, and X-ray emission from various types of jetted sources including radio-loud AGNs such as BL Lac objects, quasars, binary black holes, and X-ray binaries where active accretion results in the jet phenomenon such as in micro-quasars and other compact sources such as accreting and hence active neutron stars.

APPENDIX
RELATIONSHIP BETWEEN THE EFFECTIVE REDSHIFT
FACTOR g AND THE DOPPLER FACTOR D

The tetrads used by a local static observer in the Schwarzschild metric are given by,

$$e^\mu_{(t)} = (1 - 2M/R)^{-1/2}(1, 0, 0, 0)$$
$$e^\mu_{(r)} = (1 - 2M/R)^{1/2}(0, 1, 0, 0)$$
$$e^\mu_{(\theta)} = (1/R)(0, 0, 1, 0)$$
$$e^\mu_{(\phi)} = (1/R \sin \theta)(0, 0, 0, 1). \tag{92}$$

The directional vector $n^{(a)}$ in the GR case with light bending is given by (Pecháček et al. 2005),

$$n^{(a)} = \left(n^{(t)}, n^{(r)}, n^{(\theta)}, n^{(\phi)} \right)$$
$$= \left(1, \cos \alpha, -\frac{\sin \alpha}{\sin \psi} \cos i, \right.$$
$$\left. -\frac{\sin \alpha}{\sin \psi} \sin \phi \sin i \right). \tag{93}$$

If $\mathbf{p}$ is the four-momentum of the emitted light ray, its covariant components are given as

$$p_\mu = p_t \left(1, p_r/p_t, p_\theta/p_t, p_\phi/p_t \right), \tag{94}$$

the objective being to calculate the components p_μ in terms of the emission angles and the geometric quantities. This can be done using the relationship between the directional vector $n^{(a)}$ and p_μ given by

$$n^{(a)} = \frac{p_\mu e^\mu_{(a)}}{p_\mu e^t_{(a)}}. \tag{95}$$

Using the above equation and the tetrads from Equation (92), we obtain

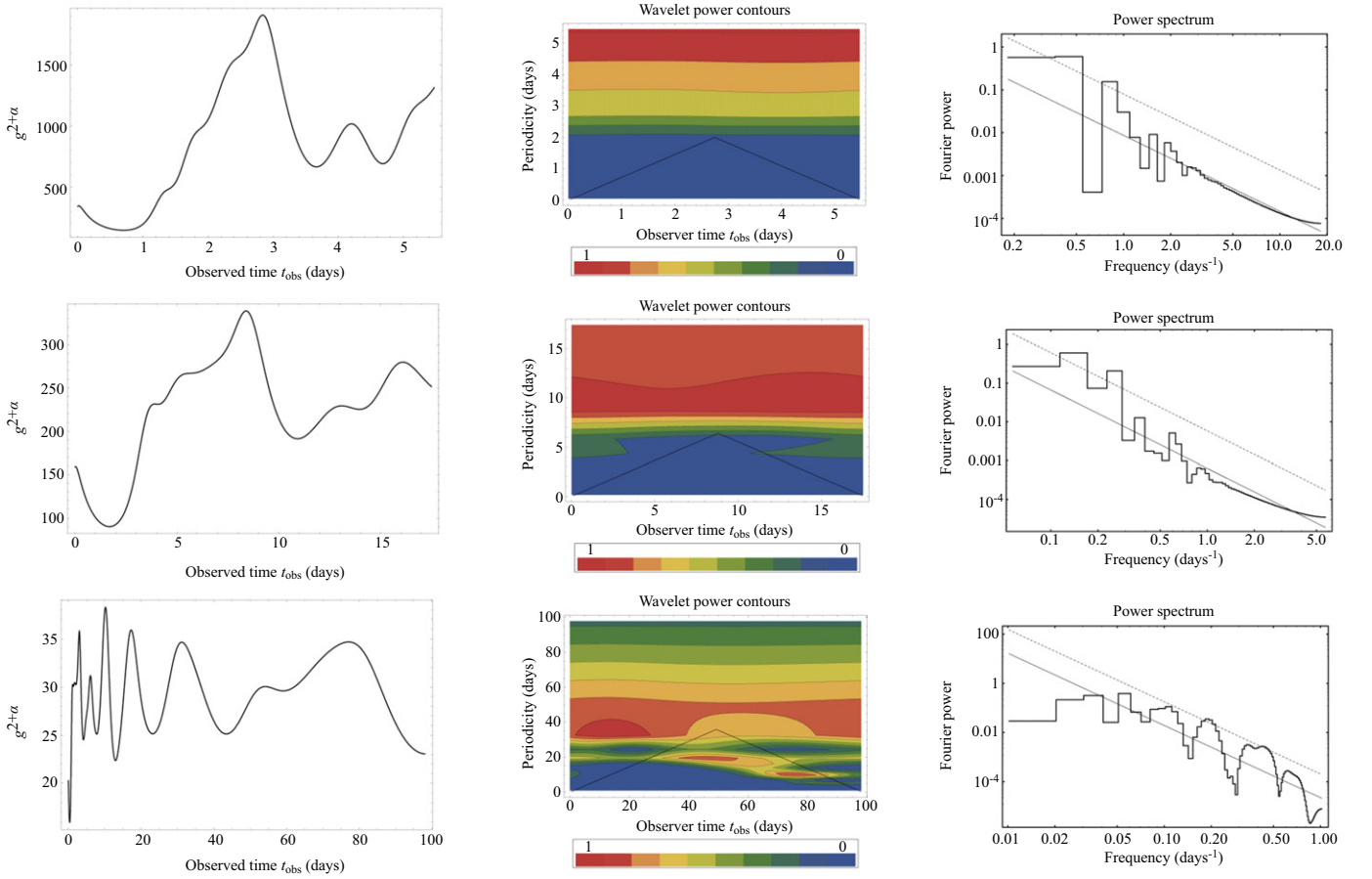$$p_r/p_t = \cos \alpha (1 - 2M/R)^{-1}$$
$$p_\theta/p_t = -\frac{\sin \alpha}{\sin \psi} \cos i R (1 - 2M/R)^{-1/2}$$
$$p_\phi/p_t = -\frac{\sin \alpha}{\sin \psi} \sin \phi \sin i R \sin \theta$$
$$\times (1 - 2M/R)^{-1/2} \tag{96}$$

The four velocity of the emitting source is given by

$$\mathbf{u} = u^t \left(1, \beta_r, \beta_\theta, \beta_\phi \right), \tag{97}$$

where $u^t = \gamma_{jet}$ is obtained from Equation (35). The effective redshift factor g is the ratio of observed to emitted energy of the photon and is given by

$$g = \frac{E_{observed}}{E_{emitted}} = \frac{\mathbf{p}(\infty) \cdot \mathbf{u}(\infty)}{\mathbf{p} \cdot \mathbf{u}} = \frac{-1}{p_\mu u^\mu}. \tag{98}$$

Figure 13. Results for light curves from multiple emitting rings of $\varpi_0 = 5\varpi_L$ to $8\varpi_L$. The plots in the left column are the simulated combined light curves. The plots in the middle column are their wavelet analysis and the plots in the right column are their PSD. The PSD is fit with a power law with a slope m. Top row: simulation for $i = 3°$, $M_\bullet = 5 \times 10^8\,M_\odot$, $\gamma_{jet} = 10$; a QPO of 1.37 days and a PSD slope of -1.77 are inferred from the timing analyses. Middle row: simulation for $i = 6°$, $M_\bullet = 5 \times 10^8\,M_\odot$, $\gamma_{jet} = 4$; QPOs of 4.37 and 8.74 days (harmonics) and a PSD slope of -2.12 are inferred from the timing analyses. Bottom row: simulation for $i = 15°$, $M_\bullet = 5 \times 10^7\,M_\odot$, $\gamma_{jet} = 2$; a QPO of 5.45 days and a PSD slope of -2.94 are inferred from the timing analyses.

Using Equations (96) and (97) in the above equation, the effective redshift factor is given by

$$g = \frac{(1 - 2M/R)^{1/2}}{u^t} \Big((1 - 2M/R)^{1/2}$$
$$- \cos\alpha \frac{\beta_r}{(1 - 2M/R)^{1/2}} - \frac{\sin\alpha}{\sin\psi} R\beta_\theta \cos i$$
$$- \frac{\sin\alpha}{\sin\psi} R \sin\theta\beta_\phi \sin\phi \sin i \Big)^{-1}. \qquad (99)$$

The g expression can be written in terms of $\beta_{jet} \cos\xi$ with β_{jet} obtained from Equation (36) already including a correction for the frame changing from an instantaneous rest frame to a local static observer frame and $\cos\xi$ obtained from Equation (55) to give the expression for g in Equation (57). Thus,

$$g = \frac{(1 - 2M/R)^{1/2}}{\gamma_{jet}\Big(1 - \beta_{jet} \cos\xi\Big)}. \qquad (100)$$

Because p_μ can also be expressed as

$$p_\mu = \epsilon$$
$$\Big(1, b\Big(1/b^2 - 1/R^2(1 - 2M/R)\Big)^{-1/2}, p_\theta/\epsilon, b\Big), \qquad (101)$$

where ϵ is the conserved photon energy, the direction between the emitted ray and the radial direction for equatorial orbits ($\theta = \pi/2$) is given by

$$\tan\alpha = \frac{p_\mu e^\mu_{(\phi)}}{p_\mu e^\mu_{(r)}}$$
$$= \Big(b/R\Big)/\Big((1 - 2M/R))^{-1/2}b$$
$$\Big(1/b^2 - 1/R^2\Big(1 - 2M/R\Big)\Big)^{-1/2}\Big). \qquad (102)$$

Solving the above equation for $\sin\alpha$, we obtain Equation (42).

REFERENCES

Abdo, A. A., Ackermann, M., Ajello, M., et al. 2011, ApJ, 726, 43
Abramowicz, M. A., Ellis, G. F. R., & Lanza, A. 1990, ApJ, 361, 470

Beloborodov, A. M. 2002, ApJL, 566, L85
Brandenburg, A., Nordlund, A., Stein, R. F., & Torkelsson, U. 1995, ApJ, 446, 741
Camenzind, M., & Krockenberger, M. 1992, A&A, 255, 59
Doeleman, S. S., Fish, V. L., Schenck, D. E., et al. 2012, Sci, 338, 355
Fendt, C., & Memola, E. 2001, A&A, 365, 631
Fukumura, K., & Kazanas, D. 2008, ApJ, 679, 1413
Fukumura, K., Kazanas, D., & Stephenson, G. 2009, ApJ, 695, 1199
Gaur, H., Gupta, A. C., Lachowicz, P., & Wiita, P. J. 2010, ApJ, 718, 279
Gupta, A. C., Fan, J. H., Bai, J. M., & Wagner, S. J. 2008, AJ, 135, 1384
Gupta, A. C., Krichbaum, T. P., Wiita, P. J., et al. 2012, MNRAS, 425, 1357
Hagen-Thorn, V. A., Larionov, V. M., Jorstad, S. G., et al. 2008, ApJ, 672, 40
Horák, J., & Karas, V. 2006, PASJ, 58, 203
Iguchi, S., Okuda, T., & Sudou, H. 2010, ApJL, 724, L166
Kudryavtseva, N. A., Britzen, S., Witzel, A., et al. 2011, A&A, 526, A51
Lachowicz, P., Gupta, A. C., Gaur, H., & Wiita, P. J. 2009, A&A, 506, L17
Liu, H., Wang, J., Mao, Y., & Wei, J. 2010, ApJL, 715, L113
Mangalam, A., & Mohan, P. 2015, JApA, 35, 431
Mangalam, A. V., & Wiita, P. J. 1993, ApJ, 406, 420
Markoff, S., Nowak, M. A., & Wilms, J. 2005, ApJ, 635, 1203
Marscher, A. P., & Gear, W. K. 1985, ApJ, 298, 114
Marscher, A. P., Jorstad, S. G., D'Arcangelo, F. D., et al. 2008, Natur, 452, 966
Mohan, P. 2014, PhD thesis, Indian Institute of Engineering Science and Technology
Mohan, P., & Mangalam, A. 2014, ApJ, 791, 74
Mohan, P., Mangalam, A., Chand, H., & Gupta, A. C. 2011, JApA, 32, 117
Mohan, P., Mangalam, A., & Chattopadhyay, S. 2014, JApA
Novikov, I. D., & Thorne, K. S. 1973, in Black Holes (Les Astres Occlus), ed. C. Dewitt, & B. S. Dewitt (Paris: Gordon & Breach), 343
Pecháček, T., Dovčiak, M., Karas, V., & Matt, G. 2005, A&A, 441, 855
Poutanen, J., & Beloborodov, A. M. 2006, MNRAS, 373, 836
Pushkarev, A. B., Kovalev, Y. Y., Lister, M. L., & Savolainen, T. 2009, A&A, 507, L33
Qian, S. J., Quirrenbach, A., Witzel, A., Krichbaum, T. P., Hummel, C. A., & Zensus, J. A. 1991, A&A, 241, 15
Rieger, F. M. 2004, ApJL, 615, L5
Shakura, N. I., & Sunyaev, R. A. 1973, A&A, 24, 337
Spruit, H. C. 1996, in Physical Processes in Binary Stars, ed. R. A. M. J. Wijers et al. (Dordrecht: Kluwer), in press arXiv:astro-ph19602022
Steffen, W., Zensus, J. A., Krichbaum, T. P., Witzel, A., & Qian, S. J. 1995, A&A, 302, 335
Torrence, C., & Compo, G. P. 1998, BAMS, 79, 61
Vokrouhlicky, D., & Karas, V. 1991, A&A, 252, 835
Wagner, S. J., Witzel, A., Heidt, J., et al. 1996, AJ, 111, 2187
Wiita, P. J. 2006, in ASP Conf. Ser. 350, Blazar Variability Workshop II: Entering the GLAST Era, ed. H. R. Miller et al. (San Francisco, CA: ASP), 183
Zhang, X.-H., & Bao, G. 1991, A&A, 246, 21